~~Preparing~~ Modeling support for an extensive $\Delta^{14}CO_2$ flask sample monitoring campaign over Europe to constrain fossil CO_2 emissions

Carlos Gómez-Ortiz[1], Guillaume Monteil[1,2], Ute Karstens[3], and Marko Scholze[1]

[1]Department of Physical Geography and Ecosystem Science, Lund University, Lund, Sweden.
[2]Barcelona Supercomputing Centre (BSC), Barcelona, Spain.
[3]ICOS ERIC - Carbon Portal, Department of Physical Geography and Ecosystem Science, Lund University, Lund, Sweden.

Correspondence: Carlos Gómez-Ortiz (carlos.gomez@nateko.lu.se)

Abstract. During 2024, an intensive $\Delta^{14}CO_2$ flask sampling campaign ~~is being~~ was conducted at 12 sampling stations across Europe as part of the CO2MVS Research on Supplementary Observations (CORSO) project. These $\Delta^{14}CO_2$ samples, combined with CO_2 atmospheric measurements, are intended to enhance the estimation of fossil CO_2 emissions over Europe through inverse modeling. In this study, we perform a series of Observing System Simulation Experiments (OSSEs) to evaluate the added value of such an intensive campaign as well as the different ~~sampling strategies in~~ flask sample selection strategies on estimating fossil fuel emissions. ~~These strategies focus on selecting samples for inversions based on their fossil CO_2 and nuclear ^{14}C composition.~~

We explore three main ~~sampling strategies~~ selection strategies and compare them against the currently more widely used method of two-week integrated samples: (1) ~~a base case scenario using a uniform sampling approach without~~ collecting flask samples every three days according to a uniform schedule, without applying specific selection criteria~~, comparing current sampling methods with the inclusion of flask samples~~; (2) ~~a strategy that selects~~ selecting flask samples with high fossil CO_2 ~~contribution~~content to better isolate anthropogenic signals; and (3) ~~a combined approach that also considers nuclear ^{14}C~~ combining fossil CO_2 selection with consideration of nuclear $^{14}CO_2$ contamination to reduce potential biases from nuclear ~~facilities. In the first strategy, the~~ emissions. The results suggest that higher sampling density ~~can improve~~ improves the estimation of fossil CO_2 emissions, particularly during periods of ~~low~~ high fossil fuel activity, such as in ~~summer. This increase in sample quantity contributes to a reduction in uncertainty , enhancing~~ winter, while integrated sampling remains more effective during summer months when emissions are lower. Increasing the number of flask samples significantly reduces uncertainty and enhances the robustness of inverse modeling results. ~~Furthermore, applying the strategy of~~ In addition, selecting samples with a high fossil CO_2 ~~contamination~~ content shows potential for improving the accuracy of emission estimates. ~~However, the most significant~~ The largest reduction in uncertainty is ~~observed when the sampling strategy also accounts for nuclear ^{14}C contamination. By considering nuclear emissions, this combined strategy helps to~~ achieved when sample selection actively avoids periods of potential high nuclear $^{14}CO_2$ contamination. This approach helps minimize potential biases, particularly in regions with ~~high nuclear activity ,~~ significant nuclear activity such as France and the UK. ~~The findings underscore~~ These findings highlight the importance of not only increasing ~~sample~~ sampling frequency but also carefully selecting samples based

on their fossil ~~and nuclear CO_2~~ CO_2 and nuclear $^{14}CO_2$ composition to improve the reliability of fossil fuel emission estimates across Europe.

1 Introduction

~~On the path to refining our understanding of carbon dynamics and the anthropogenic contributions~~ Inverse modeling has become a key tool for quantifying the anthropogenic contribution to atmospheric CO_2 levels~~, the technique of inverse modeling has emerged as a crucial tool. By integrating atmospheric observations of~~. This approach combines regular CO_2 ~~with specific tracers~~ observations with additional tracers that are sensitive to specific sources and processes. Some of these tracers are measured *in situ*~~(e.g.,~~, such as $\Delta^{14}CO_2$, CO, and APO ~~) (Basu et al., 2020; Wang et al., 2020; Chawner et al., 2024)or remotely (e.g.~~(Basu et al., 2020; Wang et al., 2020; Chawner et al., 2024), while others, like XCO_2~~) (Fischer et al., 2017; Chen et al., 2023) inverse modeling enhances the distinction between~~, are retrieved remotely (Fischer et al., 2017; Chen et al., 2023). These tracers help distinguish fossil fuel emissions ~~and~~ from natural biogeochemical fluxes, and their integration into inverse models provides stronger constraints on source attribution. A leading example ~~of such a tracer~~ is radiocarbon (^{14}C) ~~found~~ in atmospheric CO_2~~, which serves as a quantitative tracer to distinguish the fossil~~. Fossil CO_2 ~~from the biogenic component of the recently emitted CO_2 because fossil CO_2 is void of~~ lacks radiocarbon due to its decay over geological timescales (half-life of 5,730 years~~, producing a reduction of~~), leading to a measurable reduction in the radiocarbon content of ~~carbon (~~atmospheric $\Delta^{14}CO_2$ ~~) (Levin et al., 2003).~~ (Levin et al., 2003).

However, in Europe and other industrialized regions~~of the world, biogenic and~~, the ability to isolate fossil CO_2 ~~signals can be of the same order of magnitude, and because additional signal masking can occur from pure ^{14}C~~ using radiocarbon is complicated by the presence of radiocarbon emissions from nuclear ~~processes (Graven, 2015), it is necessary to have precise~~ facilities. These emissions can artificially elevate atmospheric $\Delta^{14}CO_2$ ~~measurements (Levin et al., 2020). Graven and Gruber (2011) found that in regions with a high influence of nuclear emissions such as~~ levels, masking the depletion signal caused by fossil CO_2 and potentially leading to biased estimates (Turnbull et al., 2009). For example, Graven and Gruber (2011) showed that in Europe, North America, and East Asia, radiocarbon from ~~these~~ nuclear sources can offset around 20% of the ~~fossil CO_2 dilution in ^{14}C, which can translate into a potential bias in CO_2 attributed to fossil emissions ($ffCO_2$) larger than the bias caused by exchanges with the terrestrial biosphere over~~ depletion caused by fossil emissions, leading to attribution biases that may exceed those caused by biospheric fluxes in some areas. Vogel et al. (2013), in a local application in Toronto, ~~Canada,~~ found that this offset can ~~be as high as~~ reach up to 82% of the total annual fossil CO_2 ~~emissions~~signal. A sensitivity study by Maier et al. (2023) further showed that uncorrected nuclear emissions could result in a 25% low bias in $ffCO_2$ estimates, highlighting the need for robust modeling and informed sample selection strategies.

Data on nuclear facility emissions are generally limited to annual emissions, accessible through databases such as the European Commission RAdioactive Discharges Database (RADD) (https://europa.eu/radd/index.dox, last access: 17 June 2025) or derived from energy production data from the Power Reactor Information System (PRIS) (https://pris.iaea.org/PRIS/home.aspx). These ~~data sets~~ datasets often lack the high temporal resolution necessary to identify the possible effect of large emission

events in radiocarbon samples. Studies such as those by Graven and Gruber (2011) and Zazzeri et al. (2018) provide essential emission factors and data, but also highlight the high-resolution data availability gap we just mentioned. Strict data protection policies and security measures further compound the challenge of obtaining high-resolution time series data from nuclear facilities. Few studies have directly measured and reported emissions from nuclear facilities (Akata et al., 2013; Varga et al., 2020; Lehmuskoski et al., 2021) at higher temporal resolutions, such as daily or weekly. Vogel et al. (2013) for instance, found significant deviations in interannual timescales of nuclear emissions compared to emission factors reported by Graven and Gruber (2011), but a better agreement with the long-term average observed for reactors in their study area. Most research examining the impact of nuclear emissions on $ffCO_2$ estimation is conducted in the vicinity of nuclear facilities, which allows sampling of winds directly coming from these facilities, reducing the need for high-resolution emission time series (Vogel et al., 2013; Kuderer et al., 2018). Consequently, the broader implications of nuclear emissions and their temporal variations on regional and continental scales remain less explored and understood, as evidenced in the study by Vogel et al. (2013). This localized focus limits our understanding of the impact of nuclear facility emissions on $ffCO_2$ estimations on a continental scale, such as for Europe. In addition, in inverse modeling approaches that include both CO_2 and $\Delta^{14}CO_2$, the emissions from nuclear facilities are not optimized, leading to potential inaccuracies. ~~The research~~ Research by Bozhinova et al. (2014); Graven and Gruber (2011); Turnbull et al. (2011); Zazzeri et al. (2018) demonstrates this gap, suggesting the need for more sophisticated modeling and sampling approaches to integrate nuclear emissions accurately into atmospheric inversion techniques. ~~In a sensitivity study by Maier et al. (2023), they found that nuclear emissions could lead to a 25% low-biased $ffCO_2$ estimate if not corrected for, further emphasizing the need for accurate modeling and measurements.~~

In Europe, the Integrated Carbon Observation System (ICOS) Atmosphere network continuously measures CO_2 together with other greenhouse gases (GHG) at 38 stations in Europe. Additional ~~tracers, as well as isotopes~~ atmospheric tracers, including isotopic tracers such as ^{13}C and radiocarbon (^{14}C), are measured in periodic flask samples at 17 of these ICOS stations (see ~~Figure~~ Fig. 1). Most of the stations are located in remote locations, where measurements are taken from tall towers of at least ~~100m~~ 100 m above ground level, on mountain tops, and on coastal sites (in the last two, measurements are usually taken a few meters above ground level). The objective of the network ~~stations is that the measurements~~ is to provide measurements intended to represent large areas, capturing signals ~~of~~ from sources and sinks occurring even hundreds of kilometers ~~from the station~~away. Currently, ~~^{14}C~~ radiocarbon is measured mainly in two-weekly integrated flask samples, at the highest sampling height available at each station (red and yellow dots in ~~Figure~~ Fig. 1). Since ~~2016, some stations such as Hyltemossa (HTM) in Sweden and Gartow (GAT) in Germany have been taking 1 hour ^{14}C flask samples every third day at 13:00 local time~~2015, an increasing number of ICOS stations have been collecting 1-hour flask samples regularly. Of the approximately 100 flask samples ~~that are taken at these stations during the~~ taken per station per year as quality control ~~for~~ of continuous measurements and for the analysis of other tracers and isotopes, around 25 are selected ~~to analyze~~ for $\Delta^{14}CO_2$ ~~to be used for~~ analysis to support the estimation of $ffCO_2$. Levin et al. (2020) designed a strategy to ~~choose~~ select flask samples that mainly captured large events of fossil fuel CO_2 ~~contamination~~ emissions for their posterior analysis of $\Delta^{14}CO_2$. They suggested defining a threshold for the mixing ratio of ~~the fossil fuel component CO_2 ($ffCO_2$)~~ and for the enhancement of CO (CO is a co-emmitted species from fossil fuel burning) relative to the background mixing ratio at the time the flask sample is

taken. This can be determined by near-real-time (NRT) atmospheric transport simulations (for $ffCO_2$ and ffCO) or by using continuous observations of CO at the station.

As part of the CO2MVS Research on Supplementary Observations (CORSO) project (https://www.corso-project.eu/) funded by the Horizon Europe program of the European Commission, an intensive sampling campaign of $\Delta^{14}CO_2$ ~~is~~ was carried out in 2024. In this project, flask samples are taken approximately every three days, completely dedicated to the analysis of $\Delta^{14}CO_2$ at 10 of the current ICOS sampling stations around Sweden, Germany, the Netherlands, France and the Czech Republic, complemented by two additional stations in Poland (Białystok) and England (Heathfield), and three background stations that take 2-weekly integrated samples in Ireland (Mace Head), Spain (Izaña), and Canada (Alert). Given the high analytical costs, labor intensity, and limited laboratory capacity associated with $\Delta^{14}CO_2$ measurements, implementing a sample selection strategy is essential to maximize the information gained while minimizing resource use. Identifying the most informative sampling times and locations helps optimize observational coverage, enabling more cost-effective network design without compromising the accuracy of fossil CO_2 estimates.

In this paper, we ~~investigate the impact of combining intensive~~ assess how different sample selection strategies, combining intensive flask sampling with regular integrated sampling~~for estimating~~ , can improve fossil CO_2 ~~emissions on a~~ emission estimates at subregional and subannual ~~scale~~scales. We use the ~~multi-tracer enabled~~ multi-tracer-enabled version of the Lund University Modular Inversion Algorithm (LUMIA) system ~~(Gómez-Ortiz et al., 2023) by performing~~ (Gómez-Ortiz et al., 2025) to perform a series of perfect transport ~~Observing System Simulation Experiments (OSSEs)~~OSSEs. The study aims to address three key research questions: (1) What is the added value of intensive $\Delta^{14}CO_2$ sampling compared to the current sampling done in ICOS? (2) Is there a benefit in selecting $\Delta^{14}CO_2$ flask samples based on their fossil contribution to improve fossil CO_2 emissions estimates? (3) Does further selection of flask samples based on nuclear contamination provide additional benefits when estimating fossil CO_2 emissions?

To address these questions, we calculate a series of synthetic observations by performing a forward simulation of the transport model with a set of assumed true fluxes. We then ~~select the observations based on various sampling strategies, including uniform,~~ apply different flask sample selection strategies based on fossil CO_2 ~~-based~~content, and nuclear ~~contamination-based selection criteria. Subsequently, these observations are~~ $^{14}CO_2$ contamination. These synthetic observations are subsequently inverted using LUMIA to estimate fossil CO_2 emissions, allowing us to quantify ~~the~~ differences in bias and uncertainty ~~of the different sampling strategies. This approach enables~~ associated with each selection approach. The framework and strategies presented here were developed prior to and during the early stages of the 2024 campaign to support its design and implementation. They enable a comprehensive evaluation of how ~~intensive sampling and targeted sample selection can enhance~~ increasing flask sampling frequency and accounting for both fossil and nuclear signals can improve the estimation of fossil ~~CO_2 emissions at both~~ fuel emissions at subregional and subannual scales, ultimately providing insights ~~into optimizing future sampling strategies for more accurate~~ to optimize future greenhouse gas monitoring ~~.~~ efforts.

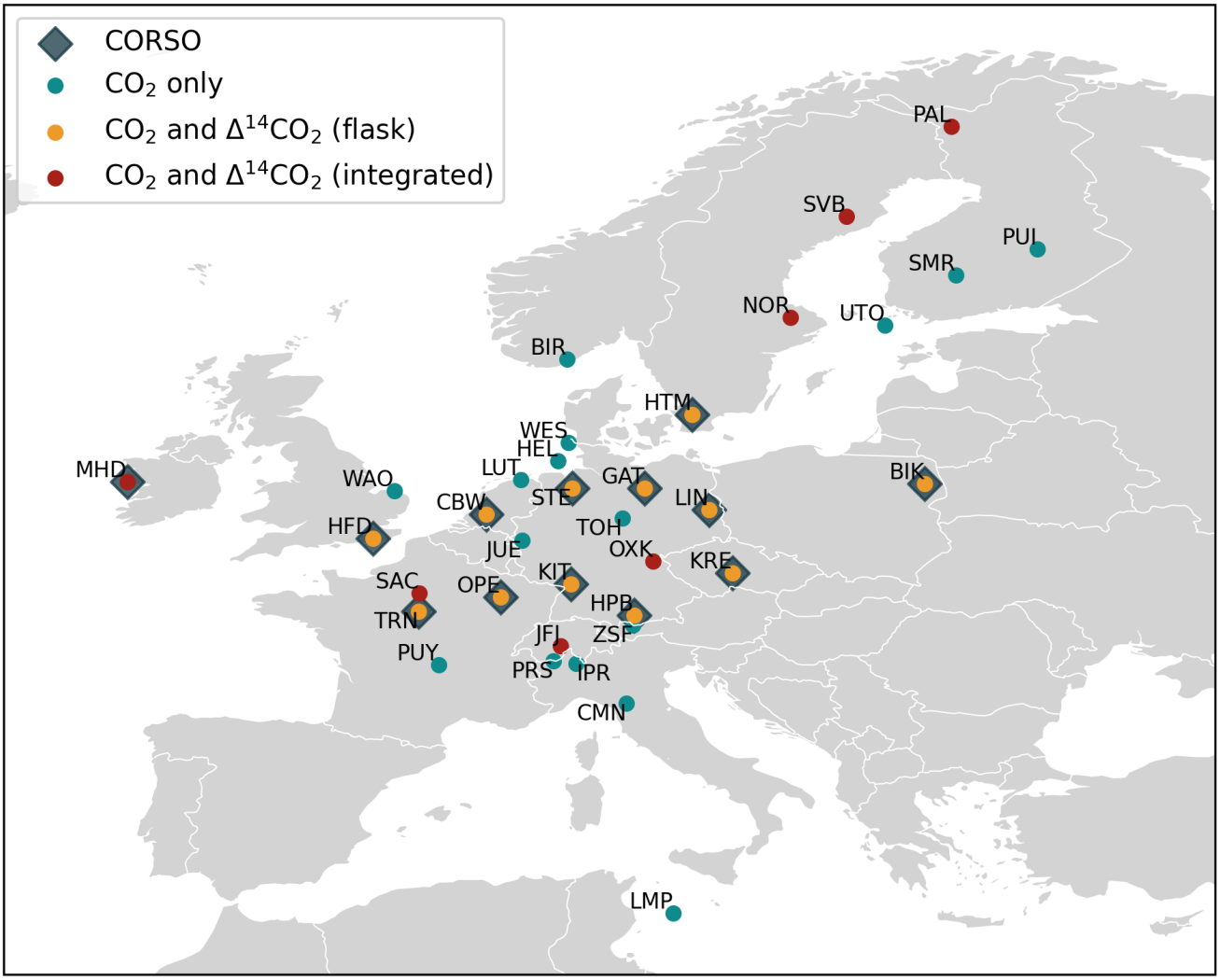

Figure 1. Sampling stations selected for this study and their identification according to the measured tracers and their participation in the CORSO project (dark blue diamonds). Green dots represent the stations where only CO_2 is measured, yellow dots where additionally $\Delta^{14}CO_2$ is measured in 1-hour flasks and red dots where $\Delta^{14}CO_2$ is measured in approximately 2-weekly integrated samples.

Table 1. Sampling ~~sites include~~ stations included in this study and $\Delta^{14}CO_2$ sampling type according to the current status and the CORSO project.

Site	Name	Country	Latitude	Longitude	Altitude (m a.s.l.)	Sampling height (m a.g.l.)	CORSO	Current $\Delta^{14}CO_2$ sampling	CORSO $\Delta^{14}CO_2$ sampling
BIK	Białystok	PL	53.2294	23.0128	183.0	300.0	X		Flask
BIR	Birkenes	NO	58.3886	8.2519	219.0	75.0			
CBW	Cabauw	NL	51.9703	4.9264	0.0	207.0	X	Integrated	Flask
CMN	Monte Cimone	IT	44.1936	10.6999	2165.0	8.0			
GAT	Gartow	DE	53.0657	11.4429	70.0	341.0	X	Integrated	Flask
HEL	Helgoland	DE	54.1804	7.8833	43.0	110.0			
HFD	Heathfield	GB	50.9770	0.2310	157.3	100.0	X		Flask
HPB	Hohenpeissenberg	DE	47.8011	11.0246	934.0	131.0	X	Integrated	Flask
HTM	Hyltemossa	SE	56.0976	13.4189	115.0	150.0	X	Integrated	Flask
IPR	Ispra	IT	45.8147	8.6360	210.0	100.0			
JFJ	Jungfraujoch	CH	46.5475	7.9851	3571.8	13.9		Integrated	
JUE	Jülich	DE	50.9102	6.4096	98.0	120.0			
KIT	Karlsruhe	DE	49.0915	8.4249	110.0	200.0	X	Integrated	Flask
KRE	Křešín u Pacova	CZ	49.5720	15.0800	534.0	250.0	X	Integrated	Flask
LIN	Lindenberg	DE	52.1663	14.1226	73.0	98.0	X	Integrated	Flask
LMP	Lampedusa	IT	35.5181	12.6322	45.0	8.0			
LUT	Lutjewad	NL	53.4036	6.3528	1.0	60.0			
MHD	Mace Head	IE	53.3261	-9.9036	5.0	24.0	X		Integrated
NOR	Norunda	SE	60.0864	17.4794	46.0	100.0		Integrated	
OPE	Observatoire pérenne de l'environnement	FR	48.5619	5.5036	390.0	120.0	X	Integrated	Flask
OXK	Ochsenkopf	DE	50.0300	11.8083	1022.0	163.0		Integrated	
PAL	Pallas	FI	67.9733	24.1157	565.0	12.0		Integrated	
PRS	Plateau Rosa	IT	45.9300	7.7000	3480.0	10.0			
PUI	Puijo	FI	62.9096	27.6549	232.0	84.0			
PUY	Puy de Dôme	FR	45.7719	2.9658	1465.0	10.0			
SAC	Saclay	FR	48.7227	2.1420	160.0	100.0		Integrated	
SMR	Hyytiälä	FI	61.8474	24.2947	181.0	125.0			
STE	Steinkimmen	DE	53.0431	8.4588	29.0	252.0	X	Integrated	Flask
SVB	Svartberget	SE	64.2560	19.7750	269.0	150.0		Integrated	
TOH	Torfhaus	DE	51.8088	10.5350	801.0	147.0			
TRN	Trainou	FR	47.9647	2.1125	131.0	180.0	X	Integrated	Flask
UTO	Utö - Baltic sea	FI	59.7839	21.3672	8.0	57.0			
WAO	Weybourne	GB	52.9500	1.1210	31.0	10.0			
WES	Westerland	DE	54.9231	8.3080	12.0	14.0			
ZSF	Zugspitze	DE	47.4165	10.9796	2666.0	3.0			

2 The LUMIA framework

We use the multi-tracer-enabled version of the Lund University Modular ~~Inverse~~ Inversion Algorithm (LUMIA) ~~(Monteil and Scholze, 2021 to perform CO_2 and $\Delta^{14}CO_2$ perfect-transport Observing System Simulation Experiments (OSSEs) for the year 2018~~ system (Gómez-Ortiz et al., 2025) to perform a series of perfect transport OSSEs covering Europe in a regional domain ranging from 15°W, 33°N to 35°E, 73°N, as shown in ~~Figure~~ Fig. 1, similar to previous regional European inverse modeling studies(Monteil et al., 2020; Thompson et al., 2020). In this case, perfect transport means that we use the same transport model to produce the synthetic observations and to perform the atmospheric inversions, as well as the same background for the synthetic observations and the modeled mixing ratios.

LUMIA is an inversion framework originally designed for regional CO_2 inversions in Europe. The framework was later extended to perform simultaneous inversions of CO_2 and $\Delta^{14}CO_2$ to estimate fossil CO_2 emissions over Europe ~~(Gómez-Ortiz et al., 2023)~~ (Gómez-Ortiz et al., 2025), which we use in this study with minor modifications detailed in this section. Since the initial release of LUMIA, it has incorporated the two-step atmospheric inversion scheme proposed by Rödenbeck et al. (2009), as thoroughly explained by Monteil and Scholze (2021). In this approach, for each observation (either CO_2 or $\Delta^{14}CO_2$), the modeled mixing ratio $\boldsymbol{y}^{\mathrm{m}}$ is described as the total of the contributions of the "foreground" $\boldsymbol{y}^{\mathrm{f}}$ (mixing ratios due to fluxes directly related with $\boldsymbol{y}^{\mathrm{m}}$ by the model, limited spatially by the domain and temporally by the length of the simulation) and the "background" $\boldsymbol{y}^{\mathrm{b}}$ (i.e., any additional contribution not captured by the foreground fluxes, including external sources or preexisting atmospheric mixing ratios):

$$\boldsymbol{y}^{\mathrm{m}} = \boldsymbol{y}^{\mathrm{b}} + \boldsymbol{y}^{\mathrm{f}} \tag{1}$$

which can be expanded for each tracer (CO_2 and $\Delta^{14}CO_2$) as:

$$\boldsymbol{y}^{\mathrm{m}}_{\mathrm{CO_2}} = \boldsymbol{y}^{\mathrm{b}}_{\mathrm{CO_2}} + \boldsymbol{y}^{\mathrm{f}}_{\mathrm{ff}} + \boldsymbol{y}^{\mathrm{f}}_{\mathrm{bio}} + \boldsymbol{y}^{\mathrm{f}}_{\mathrm{oce}} \tag{2a}$$

$$\boldsymbol{y}^{\mathrm{m}}_{\mathrm{C\Delta^{14}C}} = \underbrace{\boldsymbol{y}^{\mathrm{b}}_{\mathrm{C\Delta^{14}C}} + \boldsymbol{y}^{\mathrm{b}}_{\mathrm{cosmo}}}_{\text{background}} + \underbrace{\boldsymbol{y}^{\mathrm{f}}_{\Delta\mathrm{ff}} + \boldsymbol{y}^{\mathrm{f}}_{\Delta\mathrm{bio}} + \boldsymbol{y}^{\mathrm{f}}_{\Delta\mathrm{oce}} + \boldsymbol{y}^{\mathrm{f}}_{\mathrm{biodis}} + \boldsymbol{y}^{\mathrm{f}}_{\mathrm{ocedis}} + \boldsymbol{y}^{\mathrm{f}}_{\mathrm{nuc}}}_{\text{foreground}} \tag{2b}$$

where $\boldsymbol{y}^{\mathrm{m}}_{\mathrm{CO_2}}$ is the modeled CO_2 mixing ratio and $\boldsymbol{y}^{\mathrm{b}}_{\mathrm{CO_2}}$ is the background CO_2 mixing ratio. On the right-hand side of Eq. 2a, $\boldsymbol{y}^{\mathrm{f}}_{\mathrm{ff}}$ is the mixing ratio within the domain due to fossil CO_2 ($\boldsymbol{F}_{\mathrm{ff}}$), $\boldsymbol{y}^{\mathrm{f}}_{\mathrm{bio}}$ the mixing ratio due to the net exchange of CO_2 between the atmosphere and terrestrial ecosystems (Net Ecosystem Exchange, NEE, hereafter biosphere flux, $\boldsymbol{F}_{\mathrm{bio}}$) , and $\boldsymbol{y}^{\mathrm{f}}_{\mathrm{oce}}$ the mixing ratio due to the net exchange of CO_2 between the atmosphere and oceans ($\boldsymbol{F}_{\mathrm{oce}}$).

All terms in Eq. 2b are in units of $CO_2 \times \Delta^{14}CO_2$ (e.g. ~~ppm‰~~ppm ‰) or $C\Delta^{14}C$ for simplification, since the values in ~~‰~~ ‰ are not additive (see Basu et al. (2016) and ~~Gómez-Ortiz et al. (2023)~~ Gómez-Ortiz et al. (2025) for additional details). In this equation, $\boldsymbol{y}^{\mathrm{m}}_{\mathrm{C\Delta^{14}C}}$ and $\boldsymbol{y}^{\mathrm{b}}_{\mathrm{C\Delta^{14}C}}$ are the modeled and background $C\Delta^{14}C$ mixing ratios, respectively. ~~$\boldsymbol{y}^{\mathrm{b}}_{\mathrm{cosmo}}$~~ $\boldsymbol{y}^{\mathrm{b}}_{\mathrm{cosmo}}$ is the $C\Delta^{14}C$

mixing ratio due to the cosmogenic production of ~~$^{14}CO_2$~~ radiocarbon in the stratosphere ($\boldsymbol{F}_{\text{cosmo}}$). ~~$\boldsymbol{y}^{\text{b}}_{\text{cosmo}}$~~ $\boldsymbol{y}^{\text{b}}_{\text{cosmo}}$ is accounted in the background ($\boldsymbol{y}^{\text{b}}_{\text{C}\Delta^{14}\text{C}}$), since LUMIA was designed to assimilate only surface fluxes. Furthermore, on a regional scale, sampling sites are considered to be similarly influenced by ^{14}C-enriched stratospheric air and its influence on tropospheric ~~^{14}C~~ radiocarbon can be neglected (Maier et al., 2023; Lingenfelter, 1963). A ~~large influence of ^{14}C cosmogenic~~ significant influence from cosmogenic radiocarbon production can be expected in ~~stations sampling close to the low~~ samples collected near the lower stratosphere (above ~~6 km~~6 km) (Turnbull et al., 2009) which is not the case for any ~~of the stations considered~~ stations in this study (see Fig. 1).

The first foreground term in Eq. 2b, $\boldsymbol{y}^{\text{f}}_{\Delta\text{ff}}$, represents the ~~C$\Delta^{14}$C mixing ratio (or dilution of it)~~ reduction in atmospheric $\Delta^{14}CO_2$ due to the ~~absence of ^{14}C in~~ addition of fossil CO_2~~. Fossil CO_2~~, which is devoid of ~~^{14}C that has decayed after being buried for millions of years ($t_{\frac{1}{2}}^{^{14}\text{C}} \approx 5730$ years), but has an impact on the atmosphere $\Delta^{14}CO_2$, diluting the existing $^{14}CO_2$ into more $^{12}CO_2$~~radiocarbon. This dilution effect is modeled by transporting a tracer, $\boldsymbol{y}^{\text{f}}_{\Delta\text{ff}}$ ~~with a value of Δ^{14}C of $-1000‰$ (which corresponds to a $^{14}C/^{12}C$ ratio of 0).~~

, assigned a $\Delta^{14}CO_2$ value of -1000 ‰, representing fossil CO_2 with no radiocarbon content relative to the atmospheric standard. The next terms, $\boldsymbol{y}^{\text{f}}_{\Delta\text{bio}}$ and $\boldsymbol{y}^{\text{f}}_{\Delta\text{oce}}$ represent the net exchange from the atmosphere with the biosphere and the ocean, respectively. The contribution of these exchanges is modeled by transporting the biosphere and ocean fluxes multiplied by the isotope signature of the current atmosphere. $\boldsymbol{y}^{\text{f}}_{\text{biodis}}$ and $\boldsymbol{y}^{\text{f}}_{\text{ocedis}}$ are the contributions due to isotopic disequilibrium. ~~The old carbon that has been stored for many years in the biosphereand the oceanhas a different isotopic signature compared to~~

The carbon exchanged between the biosphere, ocean, and atmosphere has an isotopic signature that can differ from that of the current atmosphere. ~~When this carbon is released from the source to the atmosphere (for the biospheremainly due to heterotrophic respiration), it creates disturbances in the atmospheric isotopic composition. The carbon released from the biosphere is mainly ^{14}C enriched carbon captured after the atmospheric nuclear bomb tests of the 1960s, while the ocean releases mainly~~ In the terrestrial biosphere, carbon released through heterotrophic respiration may be enriched in ^{14}C~~depleted carbonthat has been at the bottom of the ocean long enough to decay to signatures lower than the current atmosphere.~~, reflecting the elevated atmospheric radiocarbon levels that followed nuclear weapons testing in the mid-20th century (Levin and Kromer, 2004; Grave . This enrichment introduces a positive isotopic disequilibrium between biospheric fluxes and the present-day atmosphere. In contrast, the ocean can release ^{14}C-depleted carbon, especially from older subsurface waters that have been isolated from atmospheric exchange for decades, allowing radioactive decay to reduce their radiocarbon content below atmospheric levels (Sweeney et al., 2007; Graven et al., 2012). These opposing disequilibrium fluxes contribute to regional and seasonal variability in atmospheric $\Delta^{14}CO_2$.

The last term, $\boldsymbol{y}^{\text{f}}_{\text{nuc}}$, represents the contribution due to the radiocarbon emissions generated by nuclear activities ($\boldsymbol{F}_{\text{nuc}}$), mainly from nuclear ~~facilities such as nuclear~~ power plants and spent fuel reprocessing ~~plants, since the contribution of nuclear bomb tests~~ facilities. The contribution of past nuclear weapons testing is now considered ~~depleted (Levin et al., 2020)~~negligible due to its significant decline over recent decades (Kutschera, 2022), and is therefore not included.

~~As in the original~~ Following the original the original implementation of LUMIA (Monteil and Scholze, 2021), here we use the global TM5 model (Huijnen et al., 2010) to calculate the background mixing ratios ($\boldsymbol{y}^{\text{b}}$) and the Lagrangian FLEXPART

model (Pisso et al., 2019) to perform the regional transport ($\boldsymbol{y}^{\mathrm{f}}$) and the inversions. In the following sections, we explain further the implementation of the models.

2.1 Background ~~mixing ratios (~~composition from TM5~~)~~

~~Background mixing ratios are the portion of~~ The background refers to the CO_2 ~~or~~ mixing ratio and $\Delta^{14}CO_2$ ~~in the atmosphere that originates from sources outside the study~~ isotopic signature of the atmosphere at the spatial and temporal boundaries of the domain. This can be a combination of emissions transported by large-scale atmospheric circulation, regional transport from outside the domain, and air masses reentering the domain (Rödenbeck et al., 2009). In this study, we use the implementation of the background mixing ratio calculation in TM5-4DVar developed by Monteil and Scholze (2021) based on the methodology proposed by Rödenbeck et al. (2009), integrated with the implementation of TM5-4DVar to include CO_2 or $\Delta^{14}CO_2$ developed by Basu et al. (2016) (https://sourceforge.net/p/tm5/cy3_4dvar/ci/default/tree/proj/tracer/radio_co2/, last visited in August 2024). Here, we model the background mixing ratio using global optimized fluxes and an initial condition from Basu et al. (2020) for 2010. These fluxes are in a horizontal resolution of $3° \times 2°$ (25 hybrid sigma-pressure vertical levels for $\boldsymbol{F}_{\mathrm{cosmo}}$), and variable time resolutions for the individual fluxes: 1 hour for $\boldsymbol{F}_{\mathrm{ff}}$, 3 hours for $\boldsymbol{F}_{\mathrm{bio}}$ and $\boldsymbol{F}_{\mathrm{oce}}$, 1 month for $\boldsymbol{F}_{\mathrm{biodis}}$ and $\boldsymbol{F}_{\mathrm{ocedis}}$, and 1 year for $\boldsymbol{F}_{\mathrm{nuc}}$ and $\boldsymbol{F}_{\mathrm{cosmo}}$. The simulation is driven by meteorological fields from the European Centre for Medium-Range Weather Forecasts (ECMWF) ERA5 reanalysis project (Hersbach et al., 2020).

Here, we describe a ~~small modification to the original implementation~~ extension of the original setup by Monteil and Scholze (2021) to ~~account for the~~ include cosmogenic production in the background term $\boldsymbol{y}^{\mathrm{b}}_{\mathrm{C}\Delta^{14}\mathrm{C}}$ (see ~~See~~Sect. 2, Eq. 2b):

The background ~~components $\boldsymbol{y}^{\mathrm{b}}_{\mathrm{CO_2}}$ and $\boldsymbol{y}^{\mathrm{b}}_{\mathrm{C}\Delta^{14}\mathrm{C}}$ are~~ component $\boldsymbol{y}^{\mathrm{b}}_{\mathrm{t}}$, with t indicating the tracers CO_2 and $C\Delta^{14}C$, is calculated as follows:

1. ~~A~~ We perform a global forward run with TM5 to calculate the mixing ratio ~~fields $\boldsymbol{y}^{\mathrm{TM5}}_{\mathrm{CO_2}}$ and $\boldsymbol{y}^{\mathrm{TM5}}_{\mathrm{C}\Delta^{14}\mathrm{C}}$~~field $\boldsymbol{y}^{\mathrm{TM5}}_{\mathrm{t}}$, which include contributions from both inside and outside the regional domain.

2. ~~A modified~~ We then run a modified version of TM5 ~~forward run where~~ in which all fluxes and mixing ratios are set to zero ~~in all time steps~~ outside the regional domain ~~(Fig. 1) to calculate $\boldsymbol{y}^{\mathrm{f,\,TM5}}_{\mathrm{CO_2}}$.~~

3. ~~For calculating $\boldsymbol{y}^{\mathrm{f,\,TM5}}_{\mathrm{C}\Delta^{14}\mathrm{C}}$, in addition to Step 2,~~ at every time step. This produces a field $\boldsymbol{y}^{\mathrm{f,\,TM5}}_{\mathrm{t}}$, which reflects only the contribution from fluxes inside the regional domain. In this step, the cosmogenic production flux $\boldsymbol{F}_{\mathrm{cosmo}}$ is set ~~globally to zero~~ to zero globally in order to keep it ~~in~~ as part of the background in the next step.

4. The background mixing ratios are then calculated as: $\boldsymbol{y}^{\mathrm{b}}_{\mathrm{t}} = \boldsymbol{y}^{\mathrm{TM5}}_{\mathrm{t}} - \boldsymbol{y}^{\mathrm{f,\,TM5}}_{\mathrm{t}}$~~, with t indicating the tracers CO_2 and $C\Delta^{14}C$~~.

2.2 Regional transport (FLEXPART)

Following the methodology described in Monteil and Scholze (2021) and ~~Gómez-Ortiz et al. (2023)~~Gómez-Ortiz et al. (2025), our regional transport model (i.e. the operator to calculate $\boldsymbol{y}^{\mathrm{f}}$ in Equations 1 and 2) is composed of a series of pre-computed footprints with FLEXPART (Pisso et al., 2019) driven by ERA5 reanalysis data for 2018 at a spatio-temporal resolution of

0.25°~~°~~ × 0.25°~~°~~ and 1~~hour~~ h, using the Python code developed to run and post-process the footprints to be used in LUMIA (https://github.com/lumia-dev/runflex, last accessed in ~~August 2024~~July 2025). We compute two types of footprints: ~~instant or flask~~ (i) instant (or flask) footprints to simulate continuous CO_2 and CO observations~~(the latter used only for sampling selection as described in Sec. 3.5), and flask $\Delta^{14}CO_2$ samples, and~~ , and (ii) integrated footprints to simulate $\Delta^{14}CO_2$ integrated observations (see ~~Sec. ??~~Sects. 3.5 and 3.3).

We compute instant footprints from the observation time and 14 days back in time releasing 10000 particles per simulation (Monteil and Scholze, 2021), and we use the same footprint to model CO_2, CO, and $\Delta^{14}CO_2$ at the corresponding observation time and sampling station. These footprints are computed for a passive air tracer, i.e. without any atmospheric chemistry reactions. Therefore, for CO we only evaluate the regional contributions (Levin et al., 2020) without accounting for the background and reactions with other atmospheric components. For the integrated footprints, we set a fixed integration time of 2 weeks (14 days), distribute 10000 FLEXPART particles per hour over this integration period, and then simulate 14 days backward from the integration start time ~~(Gómez-Ortiz et al., 2023)~~(Gómez-Ortiz et al., 2025).

2.3 The inverse modeling ~~problem~~approach

LUMIA follows an implementation of the variational approach (4D-Var). This approach seeks to iteratively minimize the mismatch between the model output and observations ~~$\delta_{\boldsymbol{y}}$~~ $\delta_{\boldsymbol{y}}$ by optimizing the control vector $\boldsymbol{x}$. The optimization process is guided by a cost function, $J(\boldsymbol{x})$, defined as:

$$J(\boldsymbol{x}) = \frac{1}{2}\left(\boldsymbol{x}-\boldsymbol{x}^{\mathrm{b}}\right)^{T}\mathbf{B}^{-1}\left(\boldsymbol{x}-\boldsymbol{x}^{\mathrm{b}}\right) + \frac{1}{2}\left(\mathbf{H}\boldsymbol{x}-\delta_{\boldsymbol{y}}\right)^{T}\mathbf{R}^{-1}\left(\mathbf{H}\boldsymbol{x}-\delta_{\boldsymbol{y}}\right) \tag{3}$$

In this equation, $\boldsymbol{x}^{\mathrm{b}}$ represents the prior estimate of the control vector, $\mathbf{B}$ is the prior uncertainty covariance matrix, $\mathbf{R}$ is the observational uncertainty covariance matrix, and $\mathbf{H}$ is the Jacobian of the observation operator H, which includes the transport model ~~itself~~ (i.e., pre-computed footprints~~described in Sec. 2.2~~) and other ~~steps~~ components needed to express $\boldsymbol{y}$ as a function of $\boldsymbol{x}$~~(e.g., ~~, such as flux aggregation and disaggregation~~of flux components, accounting for the boundary conditions, etc.).~~ , and the incorporation of boundary conditions.

The control vector $\boldsymbol{x}$ contains the set of parameters adjustable by the inversion, which are offsets to the ~~different sources and sinks of CO_2 and $\Delta^{14}CO_2$ that we want to estimate (for this study, the~~ fossil and biosphere CO_2 fluxes ~~)~~we aim to estimate. We solve for clusters ~~that are~~ aggregated in time and space. These ~~clusters are formed~~ are defined based on the sensitivity of the observation network to emissions from different regions~~. High-resolution optimization is applied to areas directly~~ : areas with high observational coverage, such as those upwind of sampling stations, are optimized at full spatial resolution ($0.5° \times 0.5°$), while regions with lower sensitivity are ~~optimized at a coarser resolution~~grouped into coarser clusters (e.g., $5° \times 3.5°$) (Gómez-Ortiz et al., 2025).

The prior error covariance matrix ($\mathbf{B}$) is constructed in three steps. First, the variances are determined to represent the assumed spatio-temporal uncertainties of the fluxes. Next, covariances are calculated based on assumed spatial and temporal correlations, incorporating the distance between grid clusters and the time difference between flux intervals. Finally, the entire

matrix is scaled using a uniform factor to match category-specific annual uncertainty values. The formulas used for fossil CO_2 emissions differ from those used for other fluxes to account for better-known emission locations and to avoid artificially low uncertainties due to flux compensations ~~(Gómez-Ortiz et al., 2023)~~(Gómez-Ortiz et al., 2025).

The observation uncertainty matrix ($\mathbf{R}$) includes both measurement uncertainties and model representation uncertainties, which account for the model's inability to perfectly simulate observations even with accurate fluxes. Ideally, the diagonal of $\mathbf{R}$ holds the total uncertainty for each observation, while the off-diagonals represent error correlations between observations. However, since these correlations are hard to quantify, common practice is to set these error correlations (off-diagonal elements) to zero. The observation uncertainty can then be provided as a simplified observation error vector (Monteil and Scholze, 2021).

The iterative procedure works by adjusting $\boldsymbol{x}$ to minimize the cost function $J(\boldsymbol{x})$, which represents the mismatch between the model and the observations weighted by their respective uncertainties. The optimal solution is achieved when the gradient, $\nabla_x J$ approaches zero, indicating that a local minimum of the cost function ~~, $\nabla_x J$, is close to zero~~has been reached. This approach ensures that the final estimate of $\boldsymbol{x}$ provides the best possible fit to the synthetic observational data while taking into account the uncertainties in both the prior information and the observations ~~(Gómez-Ortiz et al., 2023)~~(Rayner et al., 2019).

3 Experimental design

In this paper, we focus on the implementation of perfect transport ~~Observing System Simulation Experiments (hereafter OSSEs). In OSSEs, we~~ OSSEs. We calculate a series of synthetic observations, using a set of assumed "true" fluxes ($\boldsymbol{F}^{\mathrm{t}}$), by performing a forward run of our transport model. Afterwards, using a set of "prior" fluxes, we can evaluate how well the inversion framework performs in recovering the assumed "true" fluxes. In this ~~case, perfect transport means that we use the same transport model to produce the synthetic observations and to perform the atmospheric inversions, as well as the same background for the synthetic observations and the modeled mixing ratios. In this~~ section, we describe the flux products used as true and prior fluxes (~~See~~Sect. 3.1), the calculation of the synthetic observations (~~See~~Sect. 3.3), the model setup (i.e., the information needed to construct the matrices $\mathbf{B}$ and $\mathbf{R}$ and the control vector $\boldsymbol{x}$) (~~See~~Sect. 3.4), the selection criteria of the synthetic $\Delta^{14}CO_2$ flask samples (~~See~~Sect. 3.5), and the design of the OSSEs (~~See~~Sect. 3.6).

3.1 True, prior and prescribed fluxes

The assumed true fluxes, denoted as $\boldsymbol{F}^{\mathrm{t}}$, are used to generate synthetic observations through a forward run of our transport model. For the global transport simulation, we use the posterior fluxes from Basu et al. (2020) ~~, as explained in Sec. 2.1~~(see Sect. 2.1). For the regional transport, all fluxes have a resolution of $0.5° \times 0.5°$ and 1 hour in the domain shown in ~~Figure~~ Fig. 1.

We use as true fossil CO_2 flux ($\boldsymbol{F}^{\mathrm{t}}_{\mathrm{ff}}$) a product (Koch and Gerbig, 2023) for 2018 based on the Emission Database for Global Atmospheric Research (EDGAR) version 4.3.2 emission product (Janssens-Maenhout et al., 2019) following temporal variations based on MACC-TNO Denier van der Gon et al. (2011) and with temporal extrapolations and disaggregation using the COFFEE approach (Steinbach et al., 2011). ~~For the selection of the $\Delta^{14}CO_2$ flask samples, we~~ We use a fossil CO flux

product based on the same methodology described for $\boldsymbol{F}^{t}_{ff}$. This product is later used to estimate the CO enhancement from fossil fuel combustion, used as a criterion for selecting the $\Delta^{14}CO_2$ flask samples.

As true biosphere fluxes ($\boldsymbol{F}^{t}_{bio}$), we use a simulation for 2018 ~~of~~ from the LPJ-GUESS vegetation model (Wu, 2023; Smith et al., 2014)~~, the Jena Carbo-Scope oc~~. For true ocean fluxes ($\boldsymbol{F}^{t}_{oce}$), we use the Jena CarboScope oc_v2020 product, which is based on the SOCAT ~~data set of pCO_2 observations (van der Woude et al., 2022; Rödenbeck et al., 2022, 2013)as true ocean fluxes ($\boldsymbol{F}^{t}_{oce}$), and as true~~ dataset of pCO2 observations (van der Woude et al., 2022; Rödenbeck et al., 2022, 2013). As true terrestrial and oceanic isotopic disequilibrium fluxes ($\boldsymbol{F}^{t}_{biodis}$ and $\boldsymbol{F}^{t}_{ocedis}$), we use the optimized fluxes from Basu et al. (2020), regridded to match the spatial and temporal resolution of the regional transport model. Both disequilibrium fluxes are prescribed in the experiments, and hence they are not optimized. This decision is due to the high uncertainty derived from optimizing $\boldsymbol{F}_{biodis}$, and the low ~~impact~~ influence of $\boldsymbol{F}_{oce}$ and $\boldsymbol{F}_{ocedis}$ in the study domain, as ~~we found in a previous study (Gómez-Ortiz et al., 2023)~~shown in our earlier work (Gómez-Ortiz et al., 2025). The emission products from nuclear facilities are described in detail in ~~the next section (Sec. 3.2)~~Sect. 3.2.

As prior fluxes, we use the Open-source Data Inventory for Anthropogenic CO_2 (ODIAC) (Oda et al., 2018) for 2018 (Oda and Maksyutov, 2020) to represent prior fossil CO_2 emissions ($\boldsymbol{F}_{ff}$). For prior biosphere emissions ($\boldsymbol{F}_{bio}$), we use fluxes simulated by the Vegetation Photosynthesis and Respiration Model (VPRM) (Mahadevan et al., 2008; Thompson et al., 2020) for the year 2018 (Gerbig and Koch, 2021).

3.2 Radiocarbon emissions from nuclear facilities ($\boldsymbol{F}_{nuc}$)

Nuclear ~~^{14}C~~ $^{14}CO_2$ fluxes ($\boldsymbol{F}_{nuc}$) are generally prescribed in inverse modeling studies due to the high uncertainty derived from the lack of information on temporal variability. ~~However, it has been shown in previous studies that nuclear emissions can have a large impact on the estimation of fossil CO_2 emissions (Bozhinova et al., 2014; Graven and Gruber, 2011; Turnbull et al., 2011; Zazzeri et a~~ ~~.~~For this reason, we produced two sets of nuclear fluxes: one with a temporal variability to be used as the true flux ($\boldsymbol{F}^{t}_{nuc}$), and the second one with the emissions evenly distributed throughout the year as is usual for this flux category ~~(Basu et al., 2016, 2020; Gómez-Ortiz~~ (Basu et al., 2016, 2020; Gómez-Ortiz et al., 2025). Both flux products are based on the data ~~(Storm et al., 2024) used and~~ described in Maier et al. (2023) ~~, therefore, both products have~~ and Storm et al. (2024). Therefore, they share the same annual budget and spatial distribution, ~~the latter~~ which is defined using the location of ~~the~~ nuclear facilities and aggregated over ~~the~~ a $0.5° \times 0.5°$ grid.

For the temporal distribution of $\boldsymbol{F}^{t}_{nuc}$, we use the weekly temporal profiles reported by Varga et al. (2020) for the Paks Nuclear Power Plant (NPP) in Hungary and the monthly profiles reported by Akata et al. (2013) for the Rokkasho Spent Fuel Reprocessing Plant (SFR) in Japan. Both studies reported at least three years of temporal profiles. Therefore, we assign the temporal profile by randomly selecting a time span corresponding to a year starting from a random date and then assigning it to the corresponding type of nuclear facility (NPP or SFR). We did this because we did not find any evident seasonality in the temporal profiles of these two studies, and, in addition, such temporal profiles can vary between different types of nuclear reactors. With this temporal distribution, we want to add extra variability to the nuclear contribution to atmospheric $\Delta^{14}CO_2$ and study its impact when using the prescribed flat-year nuclear emissions to estimate fossil CO_2 emissions. However, we

are aware of the differences among the types of nuclear facilities and how this can affect the temporal profile. ~~As mentioned previously, for~~ For the prescribed flux, we incorporate a flat-year nuclear emission product. This ~~approach~~ allows the inversion to follow a traditional ~~approach, yet still introduces a representation of non-perfect nuclear emissionsinto the model~~setup while still accounting for imperfect representation of nuclear emissions.

3.3 Synthetic observations

~~The background component of the synthetic observations ($\boldsymbol{y}^{b}$ in Eq. 2) is calculated as explained in Sec. 2.1 using the fluxes described in Sec. 3.1.~~ We calculate hourly mixing ratios for each sampling station. For the flask ($\Delta^{14}CO_2$) samples and the instant (CO_2) observations, the background is the model output at each observation time. For the integrated $\Delta^{14}CO_2$ samples, the background is calculated as the average of the mixing ratios ~~computed~~ from the start date of ~~the~~ sampling to the end ~~date~~ of the integration period (14 days ~~for~~ in this study).

~~With~~ Using the instant and integrated footprints ~~described in Sec. 2.2~~, we perform a forward run of ~~our regional model using~~ the regional model with the true fluxes ~~introduced in Section 3.1to generate mixing ratio~~ (see Sect. 3.1) to generate time series of CO_2, CO, and $\Delta^{14}CO_2$. ~~We use a~~ The CO flux product is based on the same methodology as the fossil CO_2 ~~product (see Sec. 3.1) to simulate the~~ flux and is used to simulate CO mixing ~~ratio and perform the $\Delta^{14}CO_2$ sample selectionfollowing the methodology described in Levin et al. (2020).~~ ratios for sample selection, following the approach of Levin et al. (2020), where elevated CO deviations from background are used as a proxy for enhanced fossil CO_2 signals.

As a final step, we add ~~a random perturbation~~ random noise to the synthetic ~~observations (~~ CO_2 and $\Delta^{14}CO_2$ ~~) without exceeding the assumed observation uncertaintyto~~ observations by drawing from a normal distribution with mean zero and a standard deviation equal to the assumed observational uncertainty. This perturbation is added to each observation to mitigate the assumption of a perfect transport model.

~~As in previous studies (Monteil and Scholze, 2021; Gómez-Ortiz et al., 2023), we~~ We select the CO_2 synthetic observations for the times of ~~the day when we can get a good model representation, as usually~~ day when the model is expected to perform well, as typically done in real atmospheric inversions. This ~~is between~~ corresponds to 11:00~~and~~ –15:00 local time (LT) ~~, when the boundary layer is most likely well-developed, for sampling locations~~ for sampling sites below 1000 ~~m.a.s.l, and between~~ ma.s.l., and 22:00~~and 2~~–02:00 LT for mountaintop ~~sampling~~ stations, when the boundary layer is ~~most~~ likely below the sampling intake and ~~the free troposphere is sampled~~ free tropospheric air is sampled (Monteil and Scholze, 2021; Gómez-Ortiz et al., 2025) .

3.4 ~~Model~~ Inversion setup

~~We use the same model setup for all the OSSEs described in Sec. 3.6. As mentioned above, in all~~ In all experiments, we optimize ~~only the fossil and biosphere CO_2 fluxes ($\boldsymbol{F}_{\text{ff}}$~~ weekly fossil and biospheric CO2 fluxes ($\boldsymbol{F}$ff and $\boldsymbol{F}_{\text{bio}}$~~, respectively~~). The control vector $\boldsymbol{x}$ is composed of clusters of 2500 grid points and weekly offsets for each flux category.

~~For the construction~~ Uncertainties are first defined at the native resolution of the prior ~~error covariance matrix $\mathbf{B}$, we assume an exponential temporal correlation of one month for both fluxes and a Gaussian spatial correlation of 200 km for $\boldsymbol{F}_{\text{ff}}$ and 500~~

km for $\boldsymbol{F}_{\text{bio}}$. We assume a prior uncertainty of fluxes (e.g. 0.5° × 0.5°, hourly) and then aggregated to match the resolution of the control vector. This ensures that regions and time periods with larger fluxes are assigned proportionally larger uncertainties, while still allowing all clusters to be adjusted by the inversion.

For fossil fuel emissions, we distribute uncertainty across grid cells using the ratio log(Daily total)/Daily total. This gives relatively more weight to low-emission regions, which often carry higher relative uncertainty, and prevents unrealistically low uncertainty values in high-emission areas. For biospheric fluxes, uncertainty is distributed in proportion to the square root of the sum of the absolute hourly fluxes within each aggregation window. This avoids underestimating uncertainty in regions or periods where net biospheric fluxes are small due to compensation between photosynthesis and respiration.

The overall prior uncertainty across the domain is set to 0.21PgC yr^{-1} (30% $\mathrm{PgC\,yr^{-1}}$ for fossil emissions (30% of the prior annual budget) for $\boldsymbol{F}_{\text{ff}}$ and 0.37PgC yr^{-1} (25% $\mathrm{PgC\,yr^{-1}}$ for biosphere fluxes (25% of the absolute prior annual budget) for $\boldsymbol{F}_{\text{bio}}$ aggregated over our European domain. For $\boldsymbol{F}_{\text{ff}}$, this uncertainty reflects the difference in the 2018 annual budget for the study domain between two commonly used fossil CO_2 emission products : EDGAR ($\boldsymbol{F}^{\text{t}}_{\text{ff}}$) and ODIAC. For $\boldsymbol{F}_{\text{bio}}$, the value represents the maximum difference between the simulations for 2018 of two ecosystem models, . These values are consistent with observed differences between fossil and biosphere model products (e.g. EDGAR vs. ODIAC, LPJ-GUESS and VPRM, observed in July due to the peak in biospheric production. However, since in a real inversion we do not have information regarding the vs. VPRM).

The spatial and temporal distribution of the emissions beyond the prior estimates, the distribution of the uncertainties is chosen arbitrarily and weighted by the magnitudes of the prior estimate. We aim for higher uncertainties where we have higher fluxes, but we also want the model to have the flexibility to adjust in areas with lower fluxes error structure in the prior covariance matrix $\mathbf{B}$ is defined using an exponential temporal correlation of one month for both fluxes, and a Gaussian spatial correlation length of 200km for fossil fluxes and 500km for biospheric fluxes. These correlation lengths reflect the structure of uncertainty in emission inventories and ecosystem processes, and are consistent with previous inversion studies in Europe (Wang et al., 2018; Monteil and Scholze, 2021; Thompson et al., 2020). In the case of $\boldsymbol{F}_{\text{ff}}$, the uncertainty is distributed by weighting the value in each grid cell by the ratio log(Daily total)/Daily total of that grid cell. For $\boldsymbol{F}_{\text{bio}}$, the uncertainty is distributed proportionally to the square root of the absolute value of each grid cell and time step.

For the construction of the observational uncertainty covariance matrix Observation uncertainties in $\mathbf{R}$, we calculate the observation errors are defined as follows: for CO_2observations, the prior error for each observation is set , we assign a prior error equal to the standard deviation of observations within a ±3.5 model-simulated concentrations within a ±3.5 day window around it, while for each observation. For $\Delta^{14}CO_2$observations (both integrated and flask samples), we use a constant value of 0.9 ppm , we assume a constant error of 0.9ppm $C\Delta^{14}C$(, equivalent to 2.15 ± 0.05‰ $\Delta^{14}CO_2$)‰.

3.5 Synthetic $\Delta^{14}CO_2$ flask sample selection

There are three key criteria for selecting We define three criteria to guide the selection of $\Delta^{14}CO_2$ flask samples : in the OSSEs: (1) samples taken at midday (midday sampling at 13:00 LT) approximately every third day, (2) samples that capture events selection of high fossil CO_2 contamination, and events, and (3) samples that avoid events of avoidance of periods

with potentially high nuclear emissions. These correspond to the three strategies described earlier but are detailed here with their specific operational implementation. Sampling at midday ensures strong atmospheric mixing, reducing model transport errors and providing stable, low-variability conditions for accurate quality control. ~~Capturing events~~ Events of high fossil CO_2 ~~emissions involves selecting samples based on thresholds for the~~ are identified using the simulated mixing ratios of fossil CO_2 and fossil CO~~. Fossil CO is~~ , the latter serving as a reliable tracer ~~of fossil~~ due to its co-emission during combustion and lack of biological sources. While these are simulated values in the OSSE framework, in real-world applications, total CO_2 ~~because it is co-emitted during combustion processes but is not influenced by biological activity (Levin et al., 2020). Avoiding~~ and total CO measurements are used in near-real time. Fossil CO_2 is then inferred from observed CO enhancements relative to a background, together with known emission ratios, as described by Levin et al. (2020). Avoiding potentially high nuclear emissions is crucial to prevent masking the fossil fuel signal with nuclear $^{14}CO_2$ emissions (Maier et al., 2023; Graven and Gruber, 2011).

For the $\Delta^{14}CO_2$ flask sample selection, we follow the same thresholds for fossil CO_2 (≥ 4~~ppm~~ ppm) and fossil CO (≥ 40 ~~ppb~~ ppb) (hereafter ffCO_2 and ffCO, respectively) as proposed by Levin et al. (2020) to capture events of high fossil CO_2 ~~contamination~~emissions. Additionally, we introduce a new threshold for nuclear CΔ^{14}C of ≤ 1~~ppm~~ ppm CΔ^{14}C to avoid capturing events of potentially high nuclear $\Delta^{14}CO_2$ contamination. This value is based on forward runs using both nuclear emission products (with and without a temporal profile). Because LUMIA calculates the individual contribution of each flux category in Equation 2 to the modeled tracer fields, these estimates are used directly to apply the sample selection strategies.

At sites not directly influenced by nuclear emissions, such as Białystok (BIK~~,~~ ; see Fig. 1 and Table 1), this threshold represents ~~87%~~ 87% of the synthetic observations at 13:00 local time for the year 2018. In contrast, at sites with high nuclear impact, such as Karlsruhe (KIT) in Germany, it represents ~~41%~~ 41% of the synthetic observations (see Fig. 2). This ~~value is an approximation based on the synthetic data and forward simulations since we do not know the real behavior and magnitude of the nuclear emissions. Since LUMIA calculates the individual contribution of each flux category in Equation 2 to the mixing ratio of their corresponding air tracer, we use these values to implement the sampling selection strategies.~~ estimate is based on simulations for 2018, when nearby nuclear facilities like Philippsburg 2 (shut down at the end of 2019) were still active. However, conditions during the CORSO campaign may differ significantly due to the shutdown of all German nuclear power plants in April 2023.

~~Approximately~~ During the CORSO sampling campaign, approximately 120 ~~$\Delta^{14}CO_2$~~ flask samples (10 per month) ~~will be taken~~ are selected at each station ~~selected during the CORSO project, ensuring an even distribution throughout the year to capture seasonal variations~~for $\Delta^{14}CO_2$ analysis. Maintaining a consistent number of samples per station and distributing them ~~evenly~~ as evenly as possible throughout the year is ~~essential, as this strategy captures comprehensive temporal coverage and accounts for seasonal changes. For this reason, we focus on selecting the most~~ desirable to reduce seasonal bias. However, this distribution is not always achievable when applying strict sampling criteria, particularly in regions or periods with frequent nuclear contamination or low fossil signals. Therefore, we prioritize synthetic samples that meet the ~~criteria in each of the OSSEs describe in the following section~~ selection thresholds in each OSSE and complete the ~~10 samples per month with synthetic samples that are close to~~ 10-per-month target with additional samples that closely match the criteria.

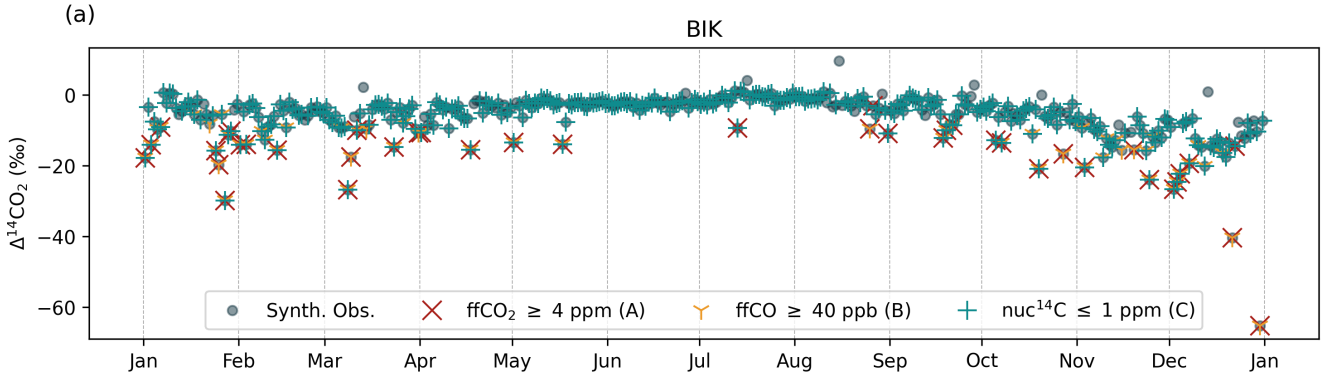

Criteria	Jan	Feb	Mar	Apr	May	Jun	Jul	Aug	Sep	Oct	Nov	Dec
A	8	3	6	2	2	0	1	3	3	4	3	7
A & B	7	3	6	2	2	0	0	1	3	3	3	6
A & C	7	3	3	2	2	0	1	1	3	3	2	5

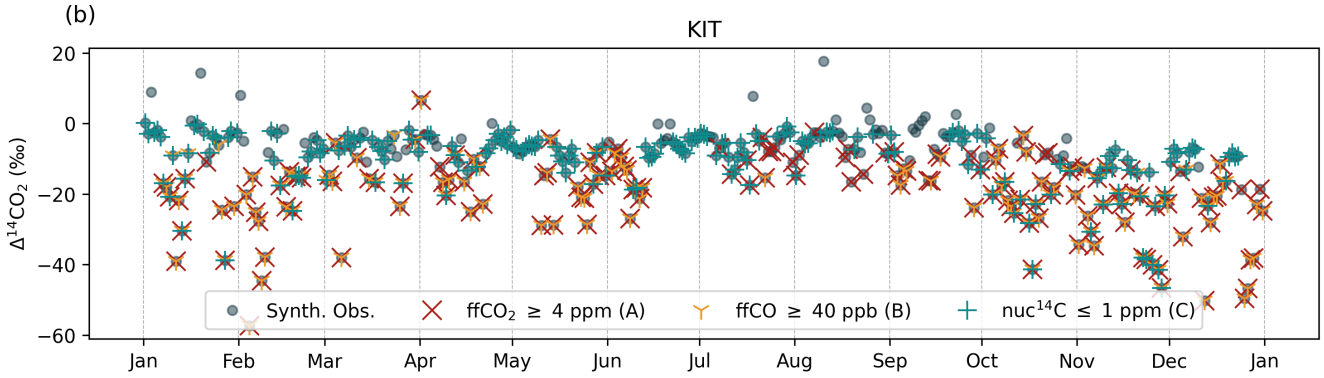

Criteria	Jan	Feb	Mar	Apr	May	Jun	Jul	Aug	Sep	Oct	Nov	Dec
A	11	14	10	11	14	11	10	8	12	23	22	18
A & B	10	14	10	10	12	10	1	0	7	20	21	15
A & C	5	5	2	2	3	2	3	1	2	9	15	1

Figure 2. Synthetic $\Delta^{14}CO_2$ flask samples at a) Białystok (BIK) and b) Karlsruhe (KIT), two of the 12 sampling sites selected for the intensive sampling campaign during the CORSO project. The time series for the remaining sampling sites can be found in Appendix A1. The tables below each figure show the number of synthetic observations per month that meet the $ffCO_2$ threshold (red cross), the $ffCO_2$ and ffCO (yellow tri) thresholds, and the $ffCO_2$ and $nuc^{14}C$ (green cross) thresholds.

3.6 Observing System Simulation Experiments (OSSEs)

In the following sections, we describe the experiments. We summarize the setup of the experiments and their criteria in Table 2. As part of the evaluation of the experiments, we calculate the posterior uncertainty of each OSSE with a Monte Carlo ensemble of 25 members. Note that small differences in the monthly prior uncertainties across figures are due to the limited size (25 members) of each Monte Carlo ensemble, despite the same annual prescribed uncertainty being applied across all regions and experiments.

3.6.1 Base case scenario (BASE)

In the first inversion, BASE, we replicate the current setup of the ICOS network using synthetic $\Delta^{14}CO_2$ integrated samples and synthetic CO_2 observations. In this experiment, we use all stations in Fig. 1 (except MHD, HFD and BIK) and integrated samples according to the column 'Current $\Delta^{14}CO_2$ sampling' in Table 1 (yellow and red dots in Fig. 1). ~~At all stations, we use~~ CO_2 observations ~~within the times~~ are used at all stations during periods of the day ~~described in Section 3.3 according to the altitude of the sampling station: midday for lowlands~~ when the atmospheric transport model is expected to perform best: midday at lowland and coastal sites, ~~midnight for~~ and midnight at mountaintop sites.

3.6.2 Including $\Delta^{14}CO_2$ flask samples (CORSO)

The selection of flask samples represents many logistic and operational challenges. The simulations and data analysis to determine if a sample meets the selection criteria are often conducted weeks after the sample has been taken. As a result, more than 10 samples need to be collected each month, which requires sufficient flasks, storage, and transport capacity. Therefore, we will begin by evaluating the use of synthetic $\Delta^{14}CO_2$ flask samples in the simplest form: taking a sample every 3 days at 13:00 local time, regardless of its composition. This experiment also works as a base case for the use of $\Delta^{14}CO_2$ flask samples. The selection in this and the following experiments is carried out in the sampling sites marked with yellow dots in Fig. 1. This is the basic approach to sampling selection in the CORSO project when it is not possible to perform near-real-time simulations to estimate the fossil or nuclear contribution of the $\Delta^{14}CO_2$ flask samples.

3.6.3 Applying fossil fuel-related thresholds ($ffCO_2$ and ffCO)

~~The subsequent experiments are designed following the thresholds described in Sec. 3.3. We do a forward run using the prior fluxes mimicking a~~ We apply the fossil fuel-related thresholds ($ffCO_2$ and ffCO) using a forward simulation with prior fluxes to approximate near-real-time ~~simulation, and based on the mixing ratios by flux category, we apply the thresholds to~~ conditions. Based on the resulting mixing ratios, we select the synthetic observations that meet the defined criteria. These thresholds are not always ~~met for all 10 observations in a month and in the case of fossil CO_2 and CO, during the summer months~~ satisfied, particularly in summer when fossil emissions are lower ~~, the thresholds are almost never met at most stations ,~~ and most stations fail to meet the minimum values. This seasonal pattern is consistent with the ~~seasonal decrease in fossil emissions, as already~~

discussed decline in fossil fuel activity during warmer months, as also noted by Levin et al. (2020). Figure 2 further illustrates the variability in meeting thresholds at different threshold fulfillment across sites.

In months where in which one of the thresholds or a combination of them is not met, we still need to select the 10 synthetic observations that best fit the experimental conditions. The first experiment including the thresholds is CORSO_ffCO2, where we select synthetic observations at 13:00 LT with a fossil CO_2 component greater than or equal to 4 ppm (see Figure Fig. 2). Generally, we select the 10 synthetic observations per month with the highest fossil CO_2 component. The second experiment is CORSO_ffCO2_ffCO (criteria A & B in Figure Fig. 2). In this experiment, when both thresholds are not neither threshold is met, we select the best combination with the highest values of $ffCO_2$ and ffCO.

3.6.4 Evaluating the impact of nuclear emissions ($nuc^{14}C$)

Here we perform two experiments, one with a low nuclear component (CORSO_In the final set of experiments, we aim to estimate the contribution of nuclear emissions to the posterior uncertainty. In a real-world application, sample selection would rely on the sensitivity of the observations to nuclear emissions (i.e., whether the upstream winds pass over a nuclear facility and coincide with a period of radiocarbon release). Although there is substantial uncertainty in the estimated magnitude of nuclear contamination, we maintain reasonable confidence in the modeled spatial and temporal patterns.

To replicate a real world scenario, we select a set of observations with low nuclear influence (CORSO_ffCO2_nuc14C) and the other with a high nuclear component (CORSO_ffCO2_nuc14C_max) while ensuring a high $ffCO_2$ compositionin both, aiming to evaluate the impact of the nuclear emissions in the estimation of fossil CO_2 emissions. In this way, we intend to completely isolate the problem by evaluating the impact solely due to nuclear emissions. Similarly to $ffCO_2$ and ffCO . We use a forward run of the prior nuclear fluxes, assumed to be evenly distributed throughout the year, to estimate the nuclear $C\Delta^{14}C$ threshold is not always met. For instance, synthetic observations at Karlsruhe (KIT) often do not meet the threshold, suggesting significant nuclear emission influences. This means that if we select the $\Delta^{14}CO_2$ flask samples every 3 days or using only the component. Since the combination of the $ffCO_2$ threshold, there is a high probability of selecting samples with a high nuclear component in sites such as KIT. In contrast, synthetic observations at Białystok (BIK) frequently meet this threshold, indicating lower nuclear emission impacts (see Fig. 2).

In CORSO_and $nuc^{14}C$ thresholds (criteria A and C in Fig. 2) is not always satisfied, we apply the following selection procedure in the CORSO_ffCO2_nuc14C (criteria A & C in Figure 2) , we follow the procedureexperiment:

1. We first select the observations that meet both the $ffCO_2$ and $nuc^{14}C$ thresholds.
2. For each site, year, and month, we then select the top 10 observations with the minimum nuclear influence lowest nuclear influence from this subset.
3. If there are less fewer than 10 observationssuch observations are available, we fill the remaining slots with observations meeting that meet the $ffCO_2$ thresholds and threshold and have moderate nuclear influence (between 1 and 2 ppm 1-2 ppm $C\Delta^{14}C$).

Table 2. Summary of the OSSEs performed in this study.

Simulation	$\Delta^{14}CO_2$ sample type	Criteria
BASE	Integrated	Current network
CORSO	Integrated and Flask	Flask samples at 13LT every third day
CORSO_\allowbreak ffCO2	Integrated and Flask	$ffCO_2 \geq 4$ppm
~~CORSO_~~CORSO_\allowbreak ffCO2 + nuclear perturbation	Integrated and Flask	$ffCO_2 \geq 4$ppm
CORSO_\allowbreak ffCO2_\allowbreak ffCO	Integrated and Flask	$ffCO_2 \geq 4$ppm & $ffCO \geq 40$ppb
CORSO_\allowbreak ffCO2_\allowbreak nuc14C	Integrated and Flask	$ffCO_2 \geq 4$ppm & $nuc^{14}C \leq 1$ppm
~~CORSO_~~CORSO_\allowbreak ffCO2_~~nuc14Cmax~~\allowbreak nuc14C + nuclear perturbation	Integrated and Flask	$ffCO_2 \geq 4$ppm & ~~$nuc^{14}C > 1$ppm~~$nuc^{14}C \leq 1$pp

4. If ~~still short of 10 observations, we fill the remaining slots with observations meeting~~ this is still insufficient, we complete the sample by selecting observations that meet only the nuclear threshold, ~~ensuring the highest possible~~ prioritizing those with the highest fossil CO_2 influence.

~~In the CORSO_~~We compare this experiment against CORSO_ffCO2, in which we do not consider the nuclear contamination. For each set of observations (CORSO_ffCO2 and CORSO_ffCO2_nuc14C~~_max experiment,~~), we ~~aim to capture the effect of high nuclear emission events by selecting observations with the highest nuclear contribution. Initially, we filter for observations that meet the $ffCO_2$ threshold but exclude those that meet the $nuc^{14}C$ threshold. These observations are then sorted by fossil and nuclear emissions, and we select the top 10 with the highest nuclear emissions for each site, year, and month. If fewer than 10 observations are available, we fill the remaining slots with observations having fossil emissions between 3 and 4 ppm $C\Delta^{14}C$, still excluding those that meet the $nuc^{14}C$ threshold. If additional observations are needed, we use all remaining observations selecting the ones with highest fossil contribution.~~

~~With these two sets of observations, we perform a separate Monte Carlo ensemble to evaluate the uncertainty in the posterior fossil CO_2 emissions associated only with the influence of nuclear emissions . For this, we randomize~~ perform two Monte Carlo ensembles. In the first, we conduct a standard ensemble in which both the control vector and the observations are perturbed according to the prescribed uncertainties. In the second ensemble, we additionally include uncertainty from nuclear emissions by modifying the observation error as follows: we perturb the true nuclear emissions ~~based on~~ using an uncertainty equal to the annual nuclear budget (0.62~~Pg~~ Pg $C\Delta^{14}C$, ~~100%),~~ 100%), and recalculate the synthetic observations~~, and perform the inversions while maintaining the same setup. This provides a comprehensive assessment of the uncertainties associated with our experimental setup and the nuclear emissions~~. We assign 100% uncertainty to the nuclear emissions due to the lack of information on their temporal distribution, following Maier et al. (2023). After this, we perform the Monte Carlo ensemble in the same way as the first. The difference between the two ensembles for each observation set represents the contribution of nuclear emissions to the posterior uncertainty.

4 Results

4.1 Characterization of the sampling sites in terms of $\Delta^{14}CO_2$

We start by analyzing and comparing the real $\Delta^{14}CO_2$ integrated samples (ICOS RI et al., 2024) with the synthetic observations at the sites selected for the intensive $\Delta^{14}CO_2$ flask sample campaign (Fig. 3 and Appendix A2). Real observations show pronounced seasonal but also episodic fluctuations in $\Delta^{14}CO_2$, such as low values during February and March in CBW (~~−16.64‰~~-16.64 ‰), OPE (~~−15.14‰~~-15.14 ‰), and KRE (~~−5.75‰~~-5.75 ‰) (black line; see Fig. 3), which also coincide with the reduction in ~~modeled observations with FLEXPART (between −7.6~~ the modeled synthetic observations (between -7.6 ‰ in CBW and ~~−5.1‰~~ -5.1 ‰ in KRE, teal line) and can be associated with the typically high fossil emissions during winter. ~~On the other hand, there are also some high values during~~ In contrast, elevated values are observed in January and February ~~in KRE (2.56‰~~at KRE (2.56 ‰) and OPE (~~6.25‰~~6.25 ‰). These ~~elevated values are primarily related to~~ high values may be primarily driven by nuclear emission enrichment~~. However, during~~ , as indicated by the simulated nuclear component (red line; see Fig. 3), which shows contributions of up to 7 ‰ at KRE and OPE during this period. During the growing season, when heterotrophic respiration is more active~~than in winter, these values can~~ , elevated values could also be influenced by ~~isotopic disequilibrium. This disequilibrium is a consequence of the radiocarbon absorbed by the biosphere during the period of elevated atmospheric ^{14}C levels following nuclear weapon tests conducted between 1945 and 1980. When this carbon is released through heterotrophic respiration, it typically has a $\Delta^{14}C$ signature that is higher than that of the current atmosphere~~terrestrial isotopic disequilibrium, as reflected in the simulated component ranging from 1 to 4 ‰.

Although the synthetic observations are calculated with non-optimized fluxes, we find certain reproducibility of the seasonal patterns at sites such as CBW where we have the best agreement between the real and synthetic observations with the highest correlation coefficient (R) and lowest mean bias deviation (MBE) (see Fig. 3), and KRE and SAC (Fig. A2) in which the synthetic observations mostly underestimate the real observations (negative MBD). Also, at some sampling stations such as JFJ and PAL, the synthetic observations do not capture the variability shown by the real observations, ~~and it~~ which is reflected in high root mean square error values (RMSE, see Fig. A2).

4.2 OSSEs

We evaluate the retrieval of fossil CO_2 emissions by comparing the assumed true values ~~derived from EDGARagainst~~ (from EDGAR) with the prior estimates ~~from ODIAC~~ (from ODIAC) and the posterior estimates ~~of the experiments described in Section 3.6. In this section, we focus the analysis on the~~ from each experiment. The analysis focuses on bias and uncertainty reduction, calculated as follows ~~:~~

$$\text{Bias reduction} = \left(1 - \frac{|\text{Posterior} - \text{Truth}|}{|\text{Prior} - \text{Truth}|}\right) \times 100 \tag{4a}$$

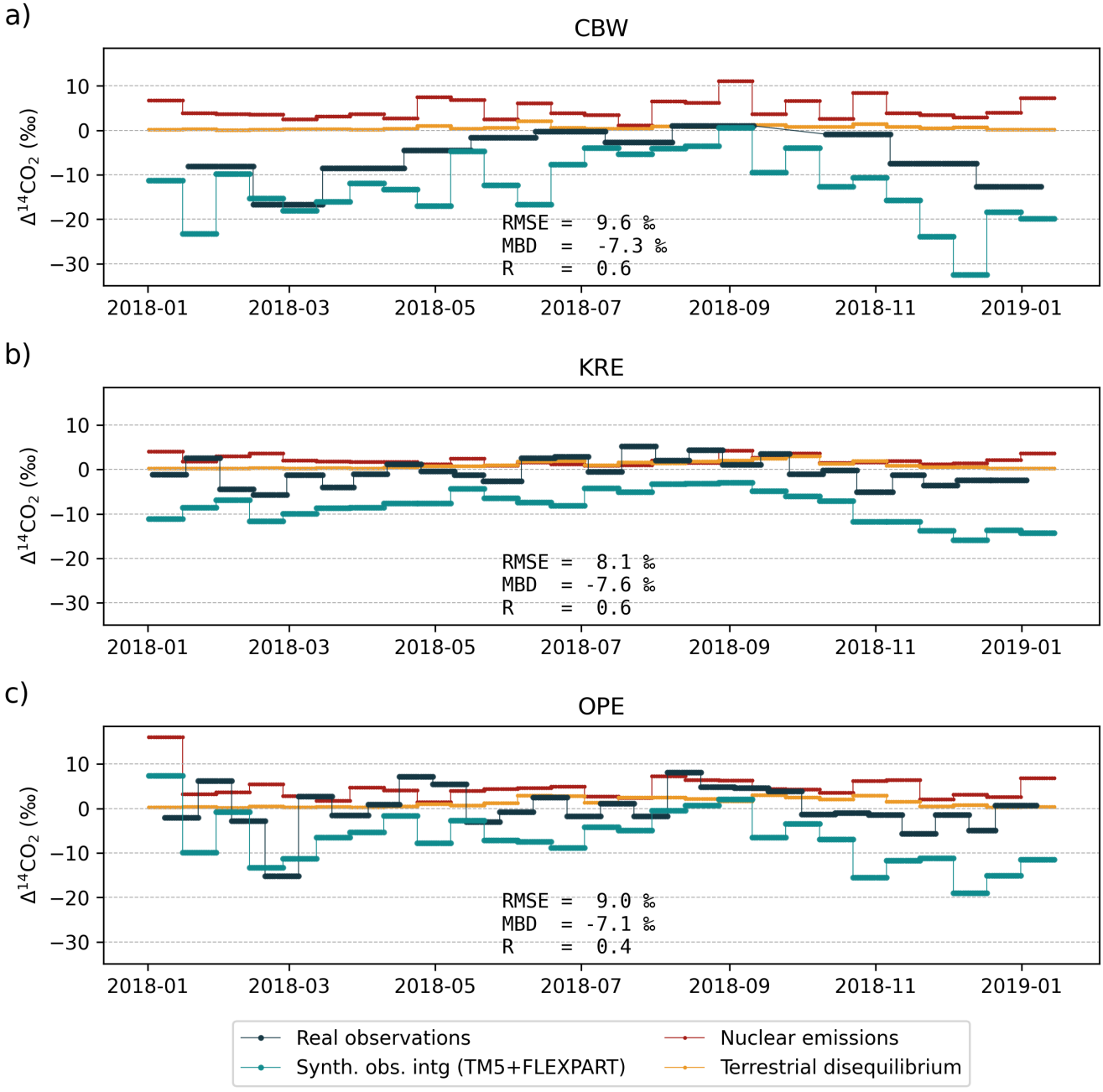

Figure 3. Comparison of the available real $\Delta^{14}CO_2$ integrated samples (black) (ICOS RI et al., 2024) with the modeled ~~background observations (red) and~~ synthetic observations (teal) at a) CBW, b) KRE and c) OPE, three of the sampling sites selected for the intensive ~~sampling~~ CORSO flask campaign. The nuclear (red) and terrestrial disequilibrium (yellow) components of the synthetic observations are also shown for comparison. Gaps in panel a reflect periods of missing integrated observations. At CBW, the integration period was approximately one month during 2018, whereas it was around 14 days at the ~~CORSO project~~other stations. Synthetic observations were modeled to match fixed 14-day integration periods across sites.

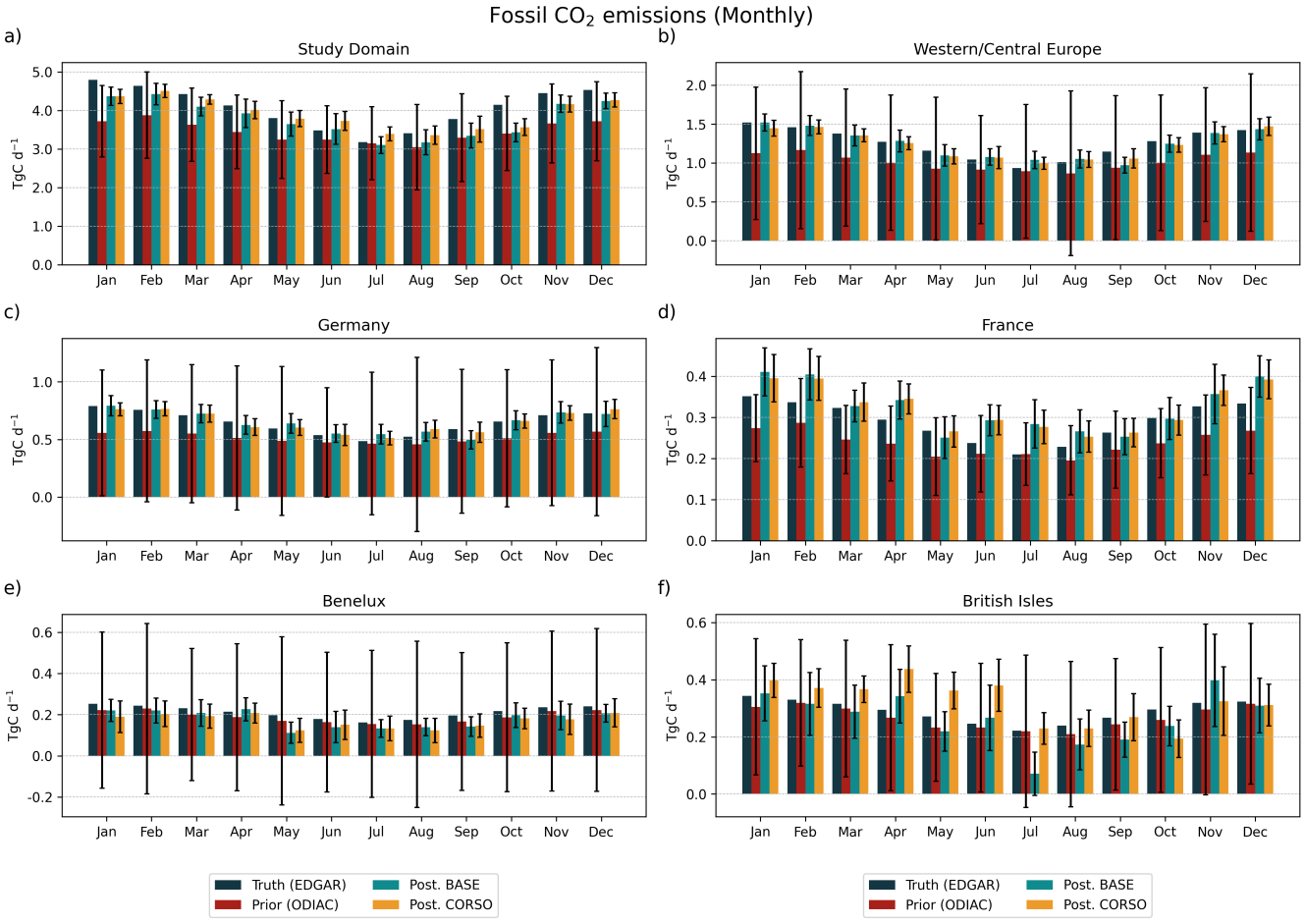

Figure 4. Monthly fossil CO_2 truth (black~~dashed lines~~), prior (red~~dotted lines~~), and posterior fluxes from the BASE (teal~~solid lines~~) and CORSO (yellow~~solid lines~~) experiments for a) the study domain and 5 sub-regions : b) Western/Central Europe, c) Germany, d) France, e) Benelux, and f) British Isles. ~~The shaded areas represent~~ Vertical error bars indicate the ~~uncertainty (1σ) calculated in~~ associated $\pm 1\sigma$ uncertainties from a Monte Carlo ensemble of 25 members. The prior uncertainty is defined independently of the inversion, while posterior uncertainties reflect the constraints imposed by the observations in each experiment.

$$\text{Uncertainty reduction} = \left(1 - \frac{\text{Posterior uncertainty}}{\text{Prior uncertainty}}\right) \times 100 \tag{4b}$$

4.2.1 Impact of adding $\Delta^{14}CO_2$ flask samples

Here, we compare the BASE and CORSO experiments. A summary of the maximum and minimum bias and uncertainty values, their respective months, and the corresponding posterior reductions is provided in Table 3. In the study domain (~~Figure~~ Fig. 4a), the true emissions ~~show a seasonal variation with peaks~~ display a clear seasonal pattern, with higher values in winter and

troughs lower values in summer, reaching a peak of 4.79 TgC day^{-1} maximum of approximately 4.8 TgC d^{-1} in January and reducing to a minimum of 3.13 TgC day^{-1} about 3.1 TgC d^{-1} in July. The prior estimates significantly underestimate (ODIAC) underestimates the true emissions throughout the year, particularly in winter months, with a bias as large as 29% in January and greater than 12% on an annual basis, with a minimum of 7% and 1% in June and July, respectively. In general, there is a larger bias reduction in the CORSO experiment with the exception of January bias of nearly 30 %. In contrast, the posterior estimates from the BASE and CORSO experiments show improved agreement with the truth. The CORSO experiment generally achieves larger reductions in bias, especially during spring and autumn. However, in June and July, where the emissionsare overestimated, with values between 22% in October and 98% in May. The BASE experiment shows a better agreement for June and July, but a lower bias reduction for October and May, with 4% and 73%, respectively. The prior uncertainty for the study domain ranges from 50% in January to 72% in August. The uncertainty reduction is similar in both experiments CORSO slightly overestimates emissions, with values ranging from 71% to 87% for CORSO , and whereas the BASE experiment provides a closer match to the true values. Prior uncertainty ranges from 71% to 75% for BASEapproximately 50 % in winter to over 70 % in summer. Both posterior experiments substantially reduce this uncertainty, with CORSO showing slightly stronger reductions, between 71 % and 87 % across the year.

WCE Western/Central Europe (WCE) and Germany, where around 30% and 16% 30 % and 16 % of the total emissions occur, respectively, have similar results in relative terms. Both regions have a larger prior bias during winter, with the largest biases occurring in January (35% 35 % for WCE and 42% 42 % for Germany). In contrast, they exhibit a lower bias in summer, with a minimum in July (5% 5 % for WCE and 4% 4 % for Germany). The posterior emissions of both experiments overestimate the monthly budgets during summer, from June to August in WCE and from May to August in Germany. However, the CORSO experiment shows values closer to the truth in this season. Outside of the summer season, the BASE experiment demonstrates a larger bias reduction in WCE, whereas the CORSO experiment shows a larger bias reduction in Germany. The prior uncertainties in both regions exceed 100% 100 % but are consistently reduced by more than 90% 90 % by the CORSO experiment in both WCE and Germany, and by more than 80% 80 % by the BASE experiment. Nevertheless, from May to September the absolute posterior uncertainty of both experiments in both regions is larger than their respective absolute prior bias.

France, the Benelux region and the British Isles have similar monthly budgetsin magnitude, with values , typically between 0.2 and 0.4TgC days^{-1}, and similar prior biases between 5% (mainly for Benelux) TgC d^{-1}, and prior biases similar to the other regions (ranging from 0 % to 31 %). However, the performance of the posterior estimates is more mixed across these regions. In France, both BASE and CORSO improve the prior estimate in early months (e.g. January–April), but during summer and autumn, especially July and November, both experiments overestimate emissions, with CORSO showing a stronger deviation from the truth. A similar pattern is observed in Benelux, where uncertainty reductions are substantial (80 %-90 %), , but posterior fluxes do not consistently reduce bias and sometimes worsen the agreement (e.g. in July and September). The British Isles exhibit the largest discrepancies: in several months (notably July, October, and November), CORSO notably overestimates emissions, and even BASE deviates from the truth. This highlights that, despite strong uncertainty reductions,

Table 3. Summary of prior relative bias and uncertainty, and posterior bias and uncertainty reductions for the BASE and CORSO experiments. All values are in percent. <0 values indicate cases where the posterior bias is greater than the prior bias. Bias and uncertainty reductions are calculated as described in Eq. 4.

Region	Prior (%)				Posterior (%)							
					BASE				CORSO			
	Rel. Bias		Rel. Uncertainty		Bias red.		Unc. red.		Bias red.		Unc. red.	
	Min.	Max.	Min.	Max.	Min.	Max.	Min.	Max.	Min.	Max.	Min.	Max.
Study Domain	1 Jul	29 Jan	25 Jan	36 Aug	<0 Jul	85 Jun	55 Jun	81 Dec	<0 Jul	98 May	71 Sep	87 Mar
Western/Central Europe	5 Jul	35 Jan	76 Jan	122 Aug	<0 Jul	100 Jan	84 Nov	89 Aug	<0 Jul	98 Feb	80 Jun	91 Feb
Germany	4 Jul	42 Jan	98 Jan	166 Aug	<0 Jul	99 Jan	84 Jun	89 Aug	<0 Jul	99 Jun	81 Jun	91 Jul
France	0 Jul	31 Mar	30 Jan	46 May	<0 Jul	98 Oct	23 Jul	60 Jun	<0 Jul	100 Sep	30 Jan	63 Sep
Benelux	4 Jul	17 Sep	159 Mar	263 Aug	<0 Sep	59 Apr	77 Jun	90 Aug	<0 Jul	74 Apr	79 Jun	86 Apr
British Isles	1 Jul	16 May	69 Feb	121 Jul	<0 Jul	78 Jan	46 Nov	73 Sep	<0 Jun	92 Sep	60 Jun	80 Mar

the posterior estimates do not always align better with the true values, particularly in regions with smaller source magnitudes or more limited observational constraints.

Overall, both BASE and CORSO experiments lead to substantial improvements over the prior by reducing bias and uncertainty in most regions. However, the differences between the two are not consistent across space and time. CORSO generally achieves greater reductions in uncertainty and improves performance in some areas, such as the core domain and Germany. In contrast, it tends to overestimate emissions in regions like France, Benelux, and ~~7%. The posterior estimates of both experiments are similar in France and~~ the ~~Benelux, with some months (May to June)having good agreement (bias reduction greater than 50%). In the case of the British Isles , there are larger differences between the posterior estimates for both experiments and less occurrences of months with bias reduction greater than 50%. With regard to the posterior uncertainties, the largest reductions are found in the Benelux with similar values for both experiments between 80% and 90%. In France and the~~ British Isles ~~, there is a larger uncertainty reduction from the CORSO experiment, with an average of 54% and 70%, respectively~~during summer and autumn. These results reflect the sensitivity of the inversion to the choice of observation sampling strategy. In the following section, we evaluate whether further selecting flask samples based on their fossil CO_2 content can improve the results.

4.2.2 Impact of selecting $\Delta^{14}CO_2$ flask samples using the $ffCO_2$ and ffCO thresholds

Here, we We compare the CORSO_ ffCO2 and CORSO_ ffCO2_ ffCO experiments against the base case, CORSO , original CORSO setup to evaluate the impact of selecting $\Delta^{14}CO_2$ flask samples using the $ffCO_2$ and ffCO fossil CO_2 and CO thresholds. This time we focus only analysis focuses on Western/Central Europe (WCE) and Germany (see Fig. 5), which show the best results in Section 4.2.1. showed the best performance in Sect. 4.2.1. Table 4 summarizes the minimum and maximum bias and uncertainty values, their respective posterior reductions, and the corresponding months.

In Western/Central Europe (WCE)WCE, the CORSO experiment generally shows a bias reduction of between 81% and 98% in winter with an uncertainty reduction of during winter months, with uncertainty reductions between 82% to 91%. The CORSO_ffCO2 experiment achieves a bias reduction of performs similarly in winter, with bias reductions ranging from 71% to 99% in winter and an uncertainty reduction and uncertainty reductions of 89%to -92%, similar to the CORSO_. CORSO_ ffCO2_ ffCO experiment with a bias reduction ffCO also shows comparable performance during winter, with bias reductions of 79%to -97% and an uncertainty reduction uncertainty reductions of 81%to -94%for the same period. .

During the summer, CORSO_differences between the experiments are more pronounced. In July, CORSO_ffCO2_ffCO has the best bias reduction in July (78% vs. −42% and 15% from ffCO shows the largest bias reduction (78%), while CORSO and CORSO_ffCO2 show much weaker improvements (–42% and 15%, respectively), while . However, in June and August, CORSO and CORSO_ffCO2 have a betterrecovery in June and August (perform better, with bias reductions between 70% and 88%vs. 26% to , compared to 26%-56% from CORSO_for CORSO_ffCO2_ffCO). The uncertainty reduction is similar for all three experiments through the yearwith values greater than ffCO. All three experiments show similarly strong uncertainty reductions throughout the year, with values consistently above 79%.

Likewise, in Germany, the uncertainty reduction for the three experimentsis greater than In Germany, uncertainty reductions exceed 83% throughout the year.across all months for all experiments.. The largest differences in bias reduction occur between May and Augustduring summer. CORSO_ffCO2 shows the best results during this period, with a bias reduction between sperforms best between May and August, with reductions ranging from 48% in July and to 97% in June, while the other two experiments show values . In contrast, CORSO shows a reduction as low as 4% in Augustfor CORSO and 7% in July for CORSO_4% in August, and CORSO_ffCO2_ffCO. The latter, in general, shows the lowest reduction in bias during summer ffCO reaches only 7% in July. Overall, CORSO_ffCO2_ffCO tends to show the weakest summer bias reduction, with a maximum reduction of 56% of 56% in June.

In summary, while all three experiments lead to substantial improvements over the prior, selecting samples based solely on fossil CO_2, CORSO_ffCO2 provides the most consistent reductions in both bias and uncertainty, particularly during summer months, without requiring the additional CO threshold.

4.2.3 Impact of nuclear power facilities

Panels a and b of Fig.4.2.3 show the uncertainty of monthly fossil CO_2 flux estimates for Western/Central Europe and Germany, respectively. The posterior estimates from CORSO_ffCO2 and CORSO_ffCO2_nuc14Carebroadlyconsistentthroughouttheyearandsho

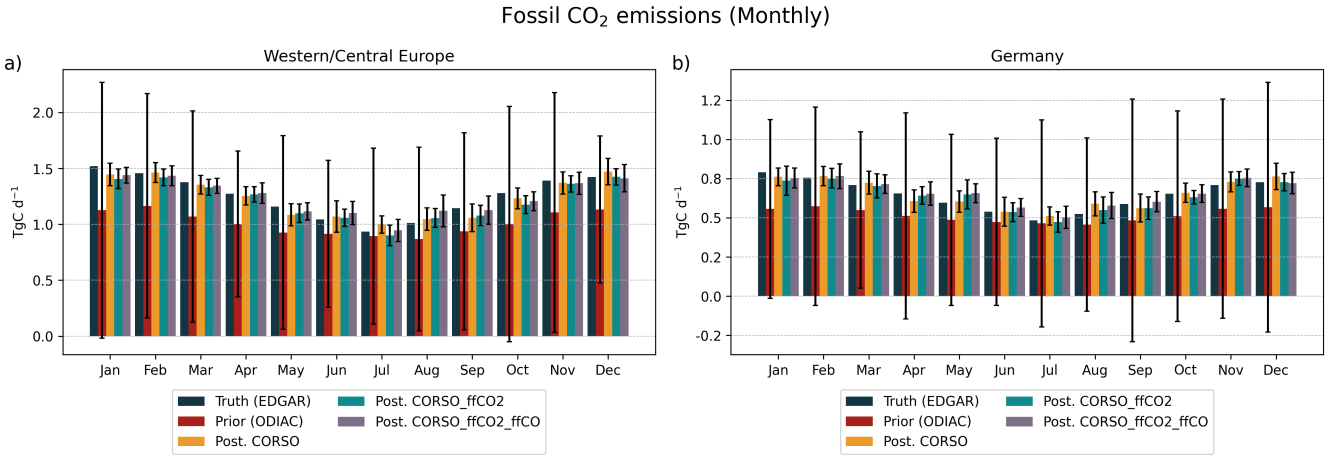

Figure 5. Monthly fossil CO_2 truth (black~~dashed lines~~), prior (red~~dotted lines~~), and posterior fluxes from the CORSO (~~teal solid lines~~yellow)~~and~~ , CORSO_ffCO2 (~~yellow solid lines~~teal), and CORSO_ffCO2_ffCO (purple~~solid lines~~) experiments for a) Western/Central Europe and b) Germany. ~~The shaded areas represent~~ Vertical error bars indicate the ~~uncertainty (1σ) calculated in~~ associated $\pm 1\sigma$ uncertainties from a Monte Carlo ensemble of 25 members.~~We excluded the prior uncertainty for a better visualization and is the same as panels b) and c) in Fig. 4.~~

Table 4. Summary of the prior bias and uncertainty and the posterior bias and uncertainty reductions for the CORSO_ffCO2 and CORSO_ffCO2_ffCO experiments. All values are in percentage.

Region	Prior (%)				Posterior (%)							
					CORSO_ffCO2				CORSO_ffCO2_ffCO			
	Rel. Bias		Rel. Uncertainty		Bias red.		Unc. red.		Bias red.		Unc. red.	
	Min.	Max.	Min.	Max.	Min.	Max.	Min.	Max.	Min.	Max.	Min.	Max.
Western/Central Europe	5 Jul	35 Jan	76 Jan	122 Aug	15 Jul	99 Dec	88 Jun	93 Nov	26 Aug	98 Apr	81 Dec	94 Jun
Germany	4 Jul	42 Jan	98 Jan	166 Aug	48 Jul	99 Dec	83 May	94 Dec	7 Jul	100 Oct	85 Aug	92 Nov

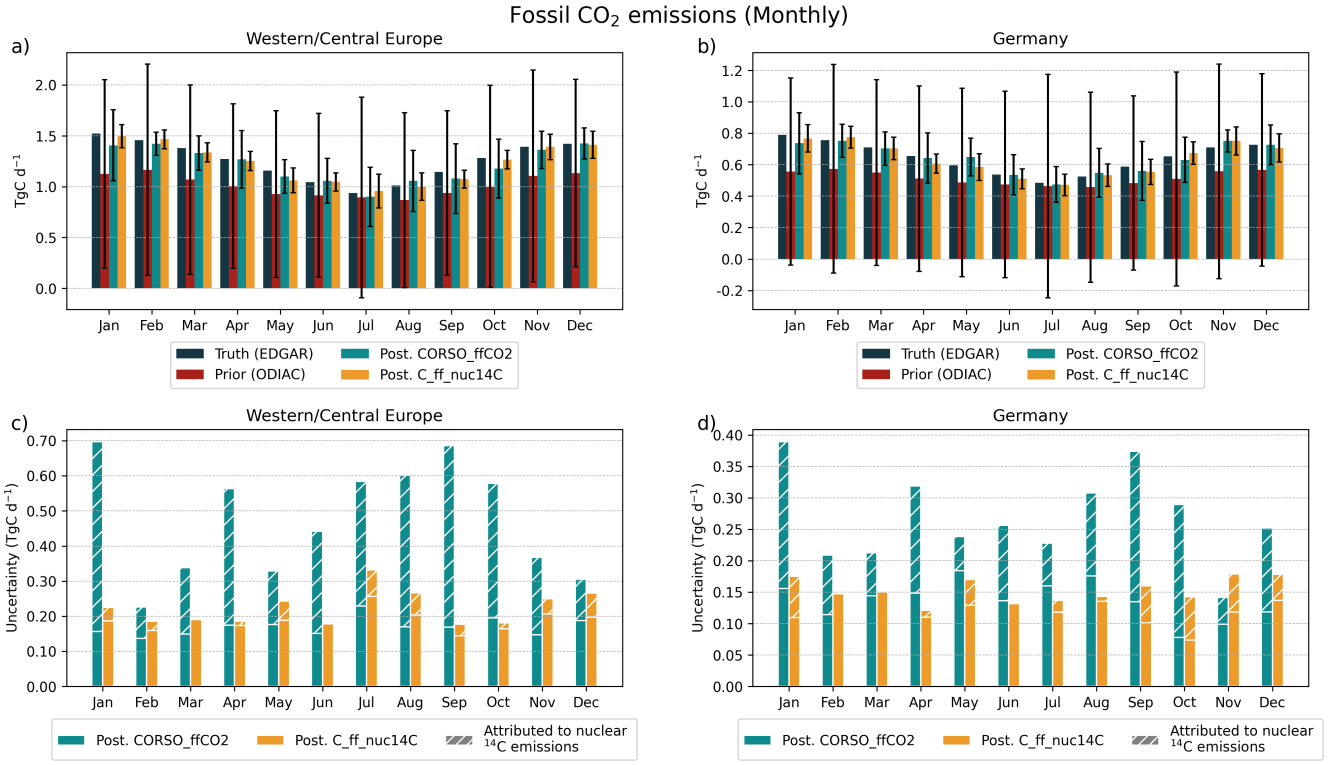

~~In Figure 4.2.3 , we show the emission time series for the CORSO~~CORSO_ffCO2 ~~_nuc14C~~ (teal) and CORSO_ffCO2_~~nuc14Cmax experiments~~ nuc14C (yellow) experiments for Western/Central Europe and Germany, respectively. Hatched segments represent the portion of posterior ~~uncertainties resulting from the Monte Carlo ensemble performed to evaluate the impact of nuclear~~ uncertainty attributed to nuclear ^{14}C emissions~~. The time series of the two experiments are very similar and close to the true emissions. However, .~~

~~In Figure 4.2.3 , we show the emission time series for the CORSO~~CORSO_ffCO2 ~~_nuc14C~~ (teal) and CORSO_ffCO2_~~nuc14Cmax experiments~~ nuc14C (yellow) experiments for Western/Central Europe and Germany, respectively. Hatched segments represent the portion of posterior ~~uncertainties resulting from the Monte Carlo ensemble performed to evaluate the impact of nuclear~~ uncertainty attributed to nuclear ^{14}C emissions~~. The time series of the two experiments are very similar and close to the true emissions. However, .~~

Figure 6. Monthly fossil CO_2 ~~emissions for the average of the~~ truth (black), prior (red), and posterior ~~values~~ fluxes from the CORSO_ffCO2 ~~_nuc14C~~ (teal), and CORSO_ffCO2_~~nuc14Cmax~~ nuc14C (yellow) experiments ~~in comparison with the truth (black-dashed) and prior (red-dotted) values~~ for a) Western/Central Europe and b) Germany. ~~The shaded areas~~ Panels c) and d) show the posterior ~~uncertainties (1σ)~~ uncertainty in fossil CO_2 flux estimates for the ~~two experiments.~~

~~In Figure 4.2.3 , we show the emission time series for the CORSO~~CORSO_ffCO2 ~~_nuc14C~~ (teal) and CORSO_ffCO2_~~nuc14Cmax experiments~~ nuc14C (yellow) experiments for Western/Central Europe and Germany, respectively. Hatched segments represent the portion of posterior ~~uncertainties resulting from the Monte Carlo ensemble performed to evaluate the impact of nuclear~~ uncertainty attributed to nuclear ^{14}C emissions~~. The time series of the two experiments are very similar and close to the true emissions. However, .~~

ffCO2_nuc14C fossil CO_2 emissions is consistently lower throughout the year, ranging from 12% to 44% in WCE and from 6% to 17% in
ffCO2_nuc14Cmax experiment (from 42% to 118% in WCE and 11% to 57% in Germany). The uncertainty reduction for the CORSO_e
620 ffCO2_nuc14C experiment is high, with more than 80% for all months in WCE, and over 88% in Germany. On the other hand, CORSO_s
ffCO2_nuc14Cmax shows the lowest uncertainty reduction from July (38%) to September (55%) in WCE and from August (70%) to Oct
ffCO2_nuc14C relative to CORSO_ffCO2 experiments is shown in Fig. **??**. The prior uncertainty highlights regions with high initial unce
ffCO2_nuc14Cmax experiment, which focuses on selecting $\Delta^{14}CO_2$ flask samples with high nuclear emissions but still in compliance wi
nuc14C (Fig.**??**f) . However, the low uncertainty reduction that we found in France for the CORSO_ffCO2_nuc14C experiment (21% agg

625 real integrated $\Delta^{14}CO_2$ samples provide evidence of high nuclear emissions, particularly during periods outside the growing season,
, who demonstrated that nuclear emissions could significantly alter the $\Delta^{14}CO_2$ signature, complicating the differentiation between fossil
further emphasized the challenges posed by nuclear emissions, highlighting that in regions with high nuclear activity, radiocarbon emissio
underscored the need to incorporate high-resolution nuclear emission data into atmospheric models to correct for these biases. In
this study, we simulate the intensive $\Delta^{14}CO_2$ flask sampling campaign during the CORSO project in under different scenarios
630 address the challenge of using atmospheric $\Delta^{14}CO_2$ measurements for the estimation of fossil CO_2 emissions in Europe, a
continent with a high concentration density of active nuclear facilities. We address thischallenge by evaluating the impact Radiocarbon emi
. To mitigate this, we evaluate the benefit of taking more samples and for shorter periods frequent, short-duration samples (1 hour
instead of 14 days) throughout the year, allowing us to capture regions and periods with high fossil emissions increasing the likelihood of c
low nuclear emissions. interference.
635 In our first experiment, we While the OSSE simulations are based on 2018 conditions, future real-world flask samples may still be influ
in 2018 to 7.8 GBq in 2021, according to the EU RADD database (https://europa.eu/radd/index.dox, last access: 17 June 2025). This incre
. Thus, despite the official shutdown of all German NPPs in April 2023, residual emissions may continue to influence $\Delta^{14}CO_2$ observatio

We first study the impact of $\Delta^{14}CO_2$ flask samples on the estimation of fossil CO_2 emissions by comparing the BASE experiment (using only integrated samples) with the CORSO experiment (including additional flask samples). Our findings
640 eal that, in general, the CORSO experiment provides a better estimation of emissions, particularly in winter months, and significantly reduces both bias and uncertainty compared to the BASE experiment. In the study domain, the CORSO experiment has a larger bias reduction and uncertainty reduction throughout most months, except for June and July, where the BASE experiment performs better. June and July are the months with the lowest fossil emissions of the year, as already found by Levin et in real observations and in this study with synthetic observations. Levin et found that fossil CO_2
645 nts are particularly rare during the summer months, with very few significant events occurring between May and August. In these months, fossil CO_2 mixing ratios rarely exceeded 4-5ppm ppm at various stations. Since integrated samples cover longer periods and hence larger areas than flask samples, they are more likely to capture the cumulative effects of low but steady emissions over time, providing a better estimate during months with fewer significant fossil CO_2 events. This extended sampling period compensates for the lower frequency of elevated emissions, ensuring that even minor contribu-
650 ns are accounted for, which may explain the improved performance of the BASE experiment during the summer months.
However, in some subregions, such as Western/Central Europe (WCE) and Germany, the CORSO experiment shows a better estimate of C

As already stated by Levin et , it is necessary to perform a sample selection of $\Delta^{14}CO_2$ flask samples to ensure a good constraint on fossil CO_2 emissions, based on the thresholds defined for CO_2 and CO. This approach helps to guarantee the detection limit of the $\Delta^{14}CO_2$ analysis, isolate fossil CO_2 signals from other sources of CO_2 and make a more efficient use of flask samples. However, this method also carries the risk of predominantly monitoring the same dominant point sources, which may not represent a comprehensive mixture for the region. To mitigate this risk, it is essential to balance the selection criteria to capture a more representative mix of regional sources. Furthermore, the uncertainty of the $\Delta^{14}CO_2$ analysis requires a minimum signal strength to ensure the accuracy of the measurements. This requires the inclusion of samples that meet the fossil ~~contamination~~ CO_2 content thresholds and provide a sufficient radiocarbon signal to reduce the analytical uncertainty. Ensuring a minimum signal strength is crucial for the reliability of the $\Delta^{14}CO_2$ data, as low signal samples can lead to higher relative errors and less confidence in fossil CO_2 estimates.

~~We applied the thresholds proposed by Levin et in two experiments, one applying $ffCO_2 \geq 4$ppm (CORSO_ffCO2), and the other com~~

The analysis of the experiments shows that there is not a single experiment that consistently outperforms the others across all seasons and regions. Although each approach (CORSO, CORSO_the selection strategy for the CORSO_ffCO2 experiments in a real-world operational setting would require performing near-real-time simulations to estimate the $ffCO_2$ component. The CO threshold was introduced because this can be obtained from continuous CO measurements, and can be calculated as the CO enhancement with respect to the background instead of ffCO (Levin et al., 2020). From the perspective of ~~Observing System Simulation Experiments (OSSEs)~~OSSEs, the results suggest that the selection of samples may not be as critical as ensuring ~~a~~ good coverage of sampling events throughout the year. The findings ~~indicate that~~ suggest that maintaining a well-distributed and frequent sampling ~~strategy might be more effective in capturing the necessary data for accurate~~ schedule provides a more representative and effective basis for accurately estimating fossil CO_2 ~~emission estimates, rather~~ emissions than relying heavily on ~~stringent~~ strict sample selection criteria. However, ~~this is not the case when we consider the selection of samples according to their nuclear contamination~~when accounting for nuclear $^{14}CO_2$ contamination, careful sample selection becomes essential to minimize biases and uncertainties.

In Europe, with more than 170 operational reactors and two reprocessing plants, nuclear contamination significantly impacts $\Delta^{14}CO_2$ samples. Maier et al. (2023) highlight that the median nuclear contamination at ICOS sites accounts for about 30% in day-and-night integrated samples and 15% in midday integrated samples, leading to substantial underestimation of fossil CO_2 estimates if not corrected. Similarly, Graven and Gruber (2011) discuss the continental-scale enrichment of atmospheric $\Delta^{14}CO_2$ due to emissions from the nuclear power industry, which creates significant gradients that extend more than ~~700km~~ 700 km from nuclear sites in Europe. Their study demonstrates that the spatial scale of these gradients is sufficient to influence regional $\Delta^{14}CO_2$ levels, requiring high-resolution data from each nuclear reactor to accurately estimate $\Delta^{14}CO_2$ enrichment and mitigate biases in fossil CO_2 estimates (Graven and Gruber, 2011).

~~Here, we investigate~~ To assess the impact of nuclear ~~emissions by performing two experiments, both following the $ffCO_2$ selection threshold, but one selecting samples with low nuclear contamination~~ contamination on fossil CO_2 estimates, we compared two sample selection experiments: one favoring low nuclear influence (CORSO_ffCO2_nuc14C) ~~, and the other~~ and one selecting samples with ~~high nuclear contamination~~ potentially high nuclear influence (CORSO_ffCO2~~_nuc14Cmax). The~~

findings show that while both experiments produce similar). While both experiments yielded emission time series that closely align with generally tracked the true emissions , the uncertainty in the CORSO_ffCO2_nuc14C experiment is consistently lower throughout the year. The CORSO_ffCO2_nuc14C experiment achieves substantial uncertainty reductions, with reductions exceeding 80% in all months in WCE and 88% in Germany. In contrast, the CORSO_ffCO2_nuc14Cmax experiment shows higher uncertainty, particularly during the summer months. Spatial analysis reveals that the CORSO_ffCO2_nuc14C experiment significantly reduces uncertainty across most of Europe, especially in well, the experiment minimizing nuclear influence consistently resulted in lower posterior uncertainties, particularly across regions with high prior uncertainty, such as Benelux, eastern Germany, eastern Franceand western England. However, countries with high nuclear emissions or regions surrounded by high nuclear emissions, such as Switzerland, France, England, and Denmark, show low uncertainty reduction in both experiments. In Switzerland, there is even a 100% increase in the posterior uncertainty when selecting samples with low nuclear contamination.

This is a very particular case in which we might see the extended effect of nuclear sites described by Graven and Gruber (2011) . In Switzerland, we only have the Jungfraujoch (JFJ) sampling station, which primarily takes integrated samples during the CORSO sampling campaign. In our simulations, JFJ is sampling emissions from nuclear facilities in Switzerland and also in neighboring Germany and France. The synthetic $\Delta^{14}CO_2$ integrated samples at this station presented enhancements due to nuclear emissionsranging from 0.04‰ to 3.28‰. The latter, corresponding to a synthetic integrated sample starting on 30 July (Fig. **??**), presented total $\Delta^{14}CO_2$ values as large as 20‰ during the Monte Carlo ensemble, mostly due to the nuclear emissions. This proximity to nuclear sites might have an impact on the estimation of fossil CO_2, leading to the observed increase in posterior uncertainty . Therefore, despite the general benefits of integrated samples in capturing France, and western Germany. This highlights the added value of targeting samples that minimize contamination from radiocarbon sources unrelated to fossil emissions. Moreover, our results show that this nuclear-related uncertainty can propagate beyond the immediate vicinity of power plants, affecting regions without nuclear facilities, such as Poland. This finding supports earlier work by Graven and Gruber (2011), who documented the regional-scale influence of European nuclear facilities on atmospheric radiocarbon measurements. These findings highlight the need to adapt sampling strategies to the spatial distribution of nuclear activity. Although integrated samples are useful for capturing long-term emission trends, in regions like Switzerland, where nuclear contamination can be a significant factor, the effectiveness of these samples can be compromised. This underscores the importance of balancing the advantages of integrated samples with the need for additional strategies to address nuclear contamination. Although the BASE experiment using only integrated samples shows some strengths in terms of uncertainty and bias reduction in periods of low fossil emissions, the utility of these samples in regions with high or surrounding nuclear emissions may be limited. This suggests that while integrated sampling can provide a solid baseline, trends, their reliability may be compromised in regions affected by nuclear facilities may require a more refined approach that combines emissions. In such cases, combining integrated and flask samplingor even performs a selection of integrated samplesto achieve reliable fossil estimates , or selectively using integrated samples, can provide a more robust approach for estimating fossil CO_2 estimation.

Integrated footprint at the Jungfraujoch (JFJ) sampling station on 30 July. Crosses indicate the location of nuclear facilities in the study domain.

In our perfect transport OSSEs implementation, we do not account for uncertainties due to transport model representation errors. Munassar et al. (2023) found that the use of different transport models, which help us to understand the model representation error, can result in differences of 0.51 $\mathrm{PgC\,yr^{-1}}$ (61%) in the posterior ~~carbon budget up to 60%~~NEE flux estimates over Europe. Their study uses continuous CO_2 observations selected at times when there is a better model representation. We ~~assume~~ note that these discrepancies~~and in general~~ , and more generally the model representation of integrated samples~~could be even worse, since the samples are continuously integrated for 2 weeks~~, may differ depending on the integration period. While short-term observations can be more sensitive to transport or mixing errors, longer integration periods (e.g. two weeks) may average out some of this variability, potentially reducing but also redistributing the associated model–data mismatches. This integration captures a mix of local and regional influences and is especially affected by diurnal circulation patterns. For example, high-altitude stations may sample polluted valley air transported upslope during the day and cleaner free tropospheric air descending at night due to mountain–valley winds. Moreover, model accuracy tends to be higher during well-mixed conditions (e.g., such as in the afternoon planetary boundary layer or in the free troposphere) compared to periods with stable stratification, such as during the nocturnal boundary layer or transition phases, which are more difficult to represent. Maier et al. (2022) study the performance of two modeling approaches using a Lagrangian model (STILT) in representing afternoon and nighttime 2-week integrated ^{14}C-based $ffCO_2$ observations from Heidelberg~~. Their standard~~ : the surface source influence (SSI) approach, similar to our ~~approach~~ implementation with FLEXPART in which all emissions are assumed to occur at ground level, ~~was almost twice better at representing integrated afternoon samples than night-time samples, when comparing modeled and observed $ffCO_2$ mixing ratios in terms of root mean square deviation (RMSD). Heidelberg is a sampling station located at 113 m.a.s.l., therefore it is expected that the models represent better the afternoon conditions when the planetary boundary layer (PBL) is well developed. They propose the~~ and the the volume source influence (VSI) approach in which there is a representation of the emission height and the plume rise of point source emissions, such as the emissions from power plants. ~~For this approach, the performance is similar for the afternoon and night samples. Exploring the model representation at the different sites, and the potential implementation of the volume source influence(VSI) approach proposed by Maier et al. (2022) to reduce the representation error under sampling conditions during an unstable atmosphere, is important for the use~~ Combining the SSI and VSI approaches, or developing hybrid frameworks that account for temporal and vertical variability in source influence, may be critical to improving the representation of integrated samples in ~~an inversion study~~ inverse modeling applications using real data.

~~The definition and characterization of the prior uncertainty is an additional limitation of our study, and this challenge may also be reflected in the posterior uncertainties observed in our experiments. A common outcome across all experiments is that, particularly during the summer months, the posterior uncertainty remains~~ In some regions, the assigned prior uncertainty exceeds 100% of the prior or true emissions (Fig. 4). This results from using relatively short spatial correlation lengths to allow the inversion to resolve emissions at finer scales, which in turn requires higher standard deviations to maintain consistent covariance structures. In practice, errors in fossil emission inventories likely exhibit broader spatial correlations, suggesting that a regionally or nationally defined uncertainty structure could be more appropriate. While our current approach may overestimate grid-scale uncertainties, it remains a reasonable approximation for testing the impact of observation strategies.

Importantly, all experiments show consistent uncertainty reductions, even though posterior uncertainties were larger than the prior bias ~~. This indicates that despite the improvements achieved through various sampling strategies, we are not yet at the point where we can reliably use estimated monthly emissions for precise fossil~~ in some regions during summer months. While this limits the resolution at which emissions can currently be reported with confidence, the consistent uncertainty reductions across all experiments highlight the potential for further improvement. Refining the prior uncertainty structure and applying the sampling strategies proposed in this study can support more accurate fossil CO_2 ~~assessments. The persistent high uncertainties during the summer underscore the need for further refinement in both the sampling strategies and~~ estimates at finer spatial and temporal scales.

In some regions, the assigned prior uncertainty exceeds 100% of the prior or true emissions (Fig.4). This results from the way the uncertainties are set up in LUMIA: the grid-cell scale uncertainties (σ_x) are scaled to match a target annual, category-specific total uncertainty over the whole domain. Therefore, the longer the spatial and temporal correlation lengths, the lower the standard deviations must be to achieve the same total variance. For fossil fuel emissions, the ~~characterization of uncertainties, as well as in the inverse modeling approach itself. Enhancing the accuracy and robustness of these models is essential to better capture the complexities of fossil CO_2 emissions, especially in seasons where the signal is weaker and more susceptible to variability. Until these challenges are addressed~~total uncertainty for Europe was based on the annual difference between the prior and the synthetic truth, derived from two independent, state-of-the-art emission inventories. The spatial correlation length was set to 200 km, under the assumption that the observation network is dense enough to resolve emission patterns at that scale. Both settings are reasonable when considered separately, but their combination leads to unrealistically large prior uncertainties at the grid-cell and even regional scale. This could be addressed by using much longer error correlation lengths, better reflecting the true ones. However, doing so would limit the use of the observation network's full potential in regions where it can resolve finer-scale patterns. Developing and testing an approach to set prior uncertainties that better balances realism in error correlations with the resolution capacity of the observation network should be a priority for future LUMIA developments. Even if the current approach is not fully optimal and limits the interpretability of some uncertainty estimates, ~~the utility of monthly emissions estimateswill remain limited, highlighting the importance of ongoing research and development in this area.~~ it still provides a valid framework for evaluating the impact of the different ^{14}C-based sampling strategies. It should not affect the relative performance of the inversions, especially in terms of error reduction. LUMIA inversions are, in general, more sensitive to the correlation structure than to the absolute uncertainty levels, particularly in regions with good observational coverage (Monteil and Scholze, 2021).

6 Conclusions

In this study, we find that adding regular $\Delta^{14}CO_2$ flask sampling to the integrated sampling (CORSO) generally provides better emission estimates than using only integrated samples (BASE), particularly during the winter months. However, the BASE experiment performed better than CORSO during low-emission months such as June and July. We also find that the selection of synthetic $\Delta^{14}CO_2$ flask samples according to their fossil contribution did not show significant improvements compared

to the simpler CORSO approach. However, when samples were selected according to their level of nuclear contamination, the experiments showed that selecting samples with low nuclear contamination led to a substantial reduction in uncertainty, particularly in regions like Western/Central Europe and Germany. In contrast, selecting samples with potentially high nuclear contamination resulted in higher uncertainties, especially during the summer months.

Therefore, we recommend ~~focusing particularly on~~ prioritizing the selection of ~~$\Delta^{14}CO_2$ flask samples according to their~~ $\Delta^{14}CO_2$ flask samples based on their potential nuclear contamination, given the limited knowledge about the temporal emission profiles of most nuclear ~~contamination given the currently unknown temporal profile of the $\Delta^{14}CO_2$ from most of the nuclear~~ facilities in our model domain. It is also necessary to perform a site-specific revision of the CO, $ffCO_2$, and $nuc^{14}C$ thresholds to adjust these values to the intensity of the fluxes measured at each station. This is also important for the $\Delta^{14}CO_2$ integrated samples. Although they can help to better estimate fossil CO_2 in periods of low emissions such as summer, long integration times can also ~~help to capture large ^{14}C nuclear emissions , which increases~~ result in large radiocarbon nuclear emissions being captured, increasing the posterior uncertainty of the estimates. In real inversions, these integrated samples can also have large representation errors. A promising approach to account for these representation error in an inversion is the implementation of the volume source influence (VSI) approach as proposed by Maier et al. (2022).

Despite the advancements shown by these experiments, high posterior uncertainties during the summer months remain a challenge. This limits the reliability of monthly emission estimates, underscoring the need for further refinement in both ~~sampling~~ selection strategies and inverse modeling techniques. Until these challenges are adequately addressed, the utility of monthly emissions estimates will remain limited, pointing to the importance of performing an appropriate uncertainty characterization of fossil emissions.

Code availability. The LUMIA source code used in this paper has been published on Zenodo and can be accessed at https://doi.org/10.5281/zenodo.8426217

Data availability. The data and the scripts used to generate the figures are available at https://github.com/cdgomezo/assets-corso-campaign.git

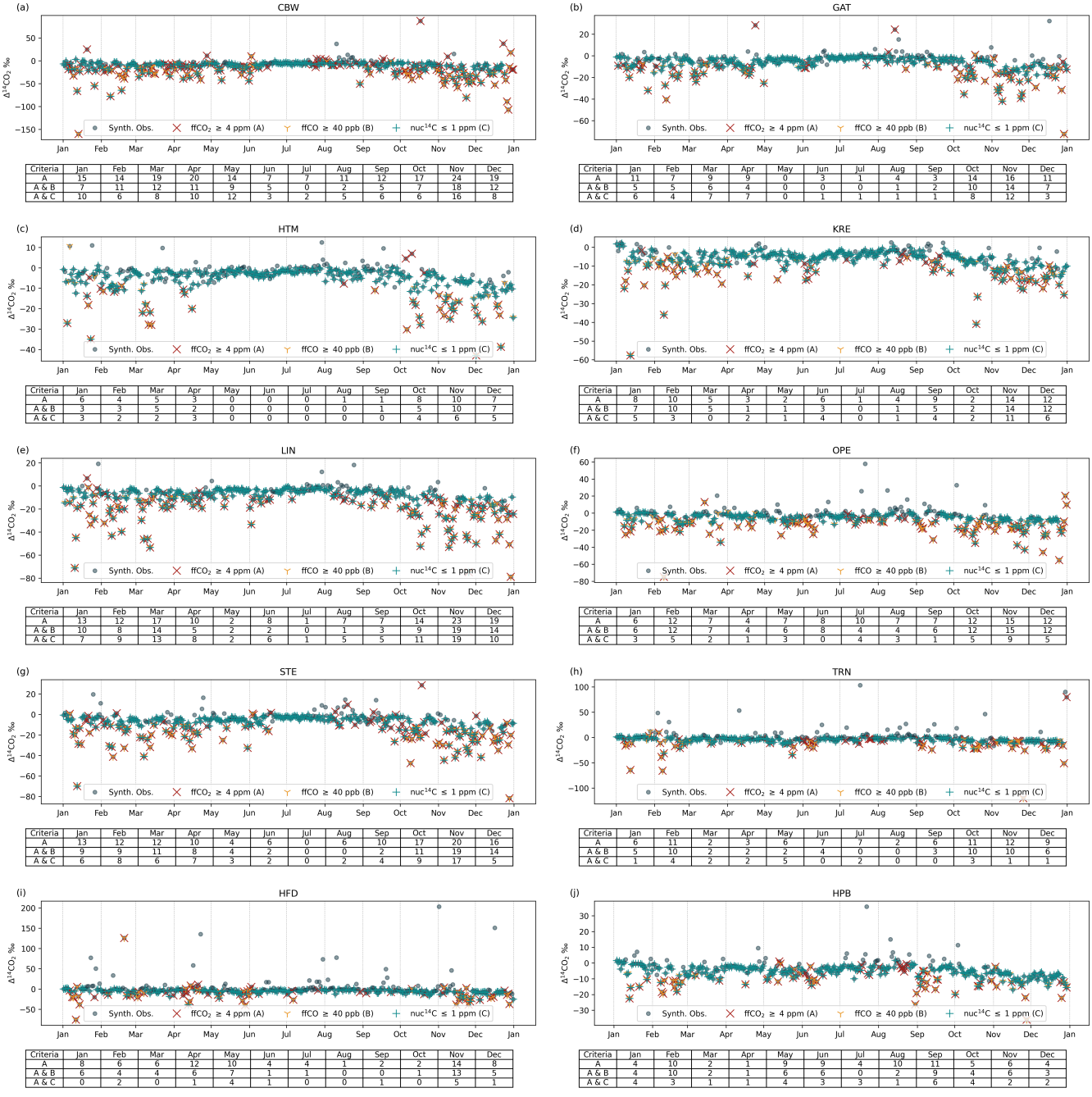

Criteria	Jan	Feb	Mar	Apr	May	Jun	Jul	Aug	Sep	Oct	Nov	Dec
A	15	14	19	20	14	7	7	11	12	17	24	19
A & B	7	11	12	11	9	5	0	2	5	7	18	12
A & C	10	6	8	10	12	3	2	5	6	6	16	8

Criteria	Jan	Feb	Mar	Apr	May	Jun	Jul	Aug	Sep	Oct	Nov	Dec
A	11	7	9	9	0	3	1	4	3	14	16	11
A & B	5	5	6	4	0	0	0	1	2	10	14	7
A & C	6	4	7	7	0	1	1	1	1	8	12	3

Criteria	Jan	Feb	Mar	Apr	May	Jun	Jul	Aug	Sep	Oct	Nov	Dec
A	6	4	5	3	0	0	0	1	1	8	10	7
A & B	3	3	5	2	0	0	0	0	1	5	10	7
A & C	3	2	2	3	0	0	0	0	0	4	6	5

Criteria	Jan	Feb	Mar	Apr	May	Jun	Jul	Aug	Sep	Oct	Nov	Dec
A	8	10	5	3	2	6	1	4	9	2	14	12
A & B	7	10	5	1	1	3	0	1	5	2	14	12
A & C	5	3	0	2	1	4	0	1	4	2	11	6

Criteria	Jan	Feb	Mar	Apr	May	Jun	Jul	Aug	Sep	Oct	Nov	Dec
A	13	12	17	10	2	8	1	7	7	14	23	19
A & B	10	8	14	5	2	2	0	1	3	9	19	14
A & C	7	9	13	8	2	6	1	5	5	11	19	10

Criteria	Jan	Feb	Mar	Apr	May	Jun	Jul	Aug	Sep	Oct	Nov	Dec
A	6	12	7	4	7	8	10	7	7	12	15	12
A & B	6	12	7	4	6	8	4	4	6	12	15	12
A & C	3	5	2	1	3	0	4	3	1	5	9	5

Criteria	Jan	Feb	Mar	Apr	May	Jun	Jul	Aug	Sep	Oct	Nov	Dec
A	13	12	12	10	4	6	0	6	10	17	20	16
A & B	9	9	11	8	4	2	0	0	2	11	19	14
A & C	6	8	6	7	3	2	0	2	4	9	17	5

Criteria	Jan	Feb	Mar	Apr	May	Jun	Jul	Aug	Sep	Oct	Nov	Dec
A	6	11	2	3	6	7	7	2	6	11	12	9
A & B	5	10	2	2	2	4	0	0	3	10	10	6
A & C	1	4	2	2	5	0	2	0	0	3	1	1

Criteria	Jan	Feb	Mar	Apr	May	Jun	Jul	Aug	Sep	Oct	Nov	Dec
A	8	6	6	12	10	4	4	1	2	2	14	8
A & B	6	4	4	6	7	1	1	0	0	1	13	5
A & C	0	2	0	1	4	1	0	0	1	0	5	1

Criteria	Jan	Feb	Mar	Apr	May	Jun	Jul	Aug	Sep	Oct	Nov	Dec
A	4	10	2	1	9	9	4	10	11	5	6	4
A & B	4	10	2	1	6	6	0	2	9	4	6	3
A & C	4	3	1	1	4	3	3	1	6	4	2	2

Figure A1. Synthetic $\Delta^{14}CO_2$ flask samples at the 10 remaining sampling sites selected for the intensive sampling campaign during the CORSO project. The tables below each figure show the number of synthetic observations per month that meet the $ffCO_2$ threshold (red cross), the $ffCO_2$ and ffCO (yellow tri) thresholds, and the $ffCO_2$ and $nuc^{14}C$ (green cross) thresholds

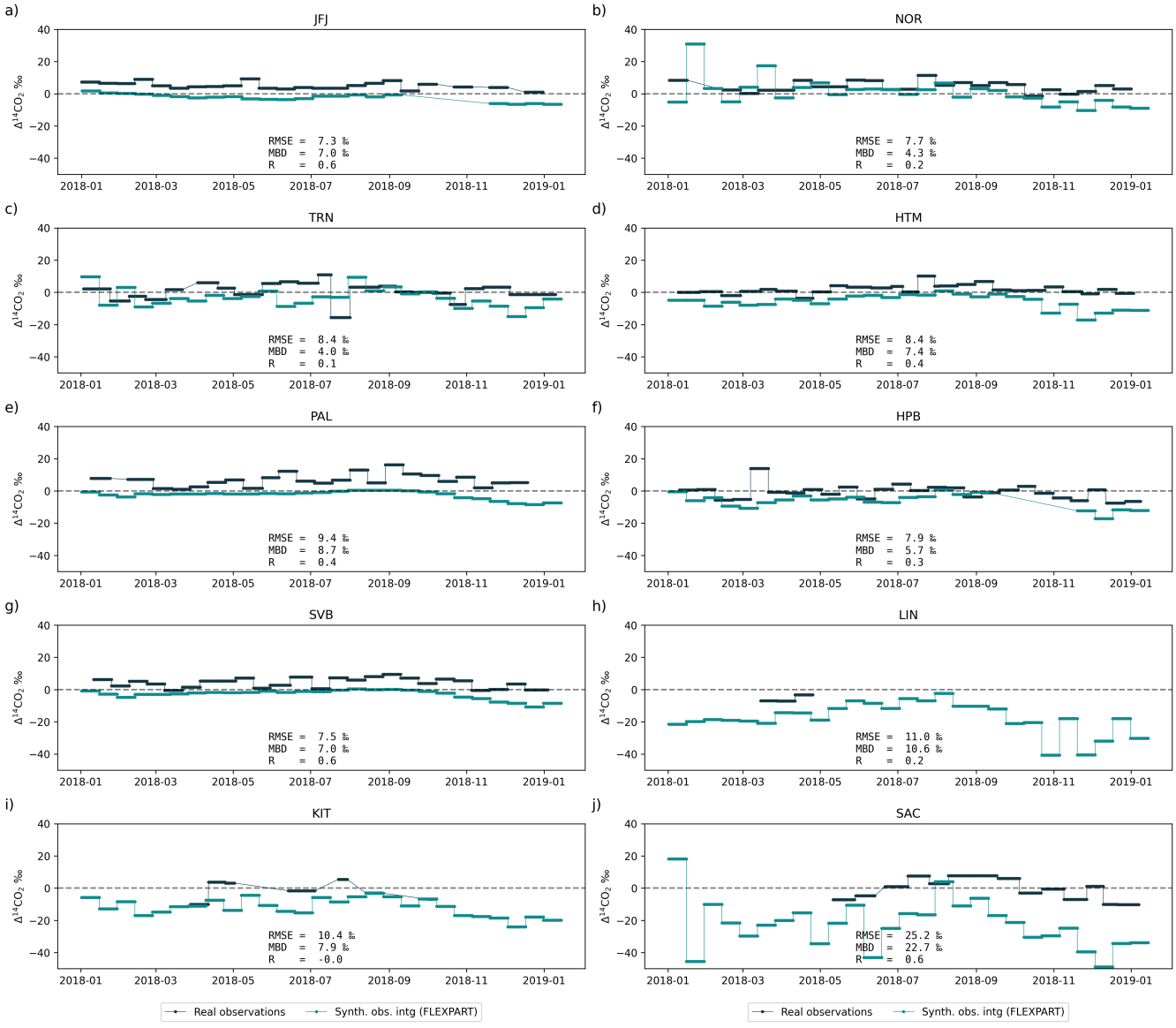

Figure A2. Comparison of the available real $\Delta^{14}CO_2$ integrated samples (black) (ICOS RI et al., 2024) with the modeled background observations (red) and synthetic observations (teal) at ten ICOS sites.

Appendix A: ~~Observations~~Additional site-level time series for $\Delta^{14}CO_2$ synthetic and observed samples

A1 Thresholds

A2 Comparison between real and modeled observations

Author contributions. All authors contributed with the design of the experiments, CG and GM developed the code, and CG performed the simulations. CG prepared the paper, and GM, UK, and MS provided corrections and suggestions for improvements.

Competing interests. The authors declare that they have no conflict of interest.

Acknowledgements. We thank the Swedish Research Council for Sustainable Development FORMAS for funding the 14C-FFDAS project (Dnr 2018-01771). We acknowledge support from the EU projects AVENGERS (Grant Agreement (GA): 101081322) and CORSO (GA: 101082194) as well as from the three Swedish strategic research areas ModElling the Regional and Global Earth system (MERGE), the e-science collaboration (eSSENCE), and Biodiversity and Ecosystems in a Changing Climate (BECC). The computations were enabled by resources provided by the National Academic Infrastructure for Supercomputing in Sweden (NAISS), the Swedish National Infrastructure for Computing (SNIC) at LUNARC, and NSC partially funded by the Swedish Research Council through grant agreements no. 2022-06725 and no. 2018-05973, and the Royal Physiographic Society of Lund through Endowments for the Natural Sciences, Medicine, and Technology - Geoscience. A special acknowledgment is given to Frank-Thomas Koch and Christoph Gerbig at the Max Planck Institute for Biogeochemistry Jena for producing and providing the fossil CO emissions product, Sourish Basu at the NASA Goddard Space Flight Center for providing the optimized fluxes used for the calculation of the background mixing ratios, and Ida Storm at the ICOS Carbon Portal for providing the annual emissions from nuclear facilities. The authors would like to thank the ICOS Central Radiocarbon Laboratory for providing the measurements of $\Delta^{14}CO_2$ in the two-week integrated ambient air samples collected at the ICOS stations Hohenpeißenberg, Hyltemossa, Jungfraujoch, Lindenberg, Norunda, Pallas, Saclay, Svartberget and Trainou.

References

Akata, N., Abe, K., Kakiuchi, H., Iyogi, T., Shima, N., and Hisamatsu, S.: Radiocarbon Concentrations in Environmental Samples Collected Near the Spent Nuclear Fuel Reprocessing Plant at Rokkasho, Aomori, Japan, During Test Operation Using Spent Nuclear Fuel, Health Physics, 105, https://journals.lww.com/health-physics/fulltext/2013/09000/radiocarbon_concentrations_in_environmental.2.aspx, 2013.

Basu, S., Miller, J. B., and Lehman, S.: Separation of biospheric and fossil fuel fluxes of CO2 by }atmospheric inversion of CO2 and 14CO2 measurements: Observation System Simulations, Atmos. Chem. Phys., 16, 5665–5683, https://doi.org/10.5194/acp-16-5665-2016, 2016.

Basu, S., Lehman, S. J., Miller, J. B., Andrews, A. E., Sweeney, C., Gurney, K. R., Xu, X., Southon, J., and Tans, P. P.: Estimating US fossil fuel CO2 emissions from measurements of 14C in atmospheric CO2, Proceedings of the National Academy of Sciences, 117, 13 300–13 307, https://doi.org/10.1073/pnas.1919032117, 2020.

Bozhinova, D., Van Der Molen, M. K., Van Der Velde, I. R., Krol, M. C., Van Der Laan, S., Meijer, H. A., and Peters, W.: Simulating the integrated summertime δ14CO2 signature from anthropogenic emissions over Western Europe, Atmospheric Chemistry and Physics, 14, 7273–7290, https://doi.org/10.5194/ACP-14-7273-2014, 2014.

Chawner, H., Saboya, E., Adcock, K. E., Arnold, T., Artioli, Y., Dylag, C., Forster, G. L., Ganesan, A., Graven, H., Lessin, G., Levy, P., Luijkx, I. T., Manning, A., Pickers, P. A., Rennick, C., Rödenbeck, C., and Rigby, M.: Atmospheric oxygen as a tracer for fossil fuel carbon dioxide: a sensitivity study in the UK, Atmospheric Chemistry and Physics, 24, 4231–4252, https://doi.org/10.5194/ACP-24-4231-2024, 2024.

Chen, H. W., Zhang, F., Lauvaux, T., Scholze, M., Davis, K. J., and Alley, R. B.: Regional CO2 Inversion Through Ensemble-Based Simultaneous State and Parameter Estimation: TRACE Framework and Controlled Experiments, Journal of Advances in Modeling Earth Systems, 15, e2022MS003 208, https://doi.org/10.1029/2022MS003208, 2023.

Denier van der Gon, H., Hendriks, C., Kuenen, J., Segers, A., and Visschedijk, A.: Description of current temporal emission patterns and sensitivity of predicted AQ for temporal emission patterns , Tech. rep., TNO, Utrecht, https://atmosphere.copernicus.eu/sites/default/files/2019-07/MACC_TNO_del_1_3_v2.pdf, 2011.

Fischer, M. L., Parazoo, N., Brophy, K., Cui, X., Jeong, S., Liu, J., Keeling, R., Taylor, T. E., Gurney, K., Oda, T., and Graven, H.: Simulating estimation of California fossil fuel and biosphere carbon dioxide exchanges combining in situ tower and satellite column observations, Journal of Geophysical Research: Atmospheres, 122, 3653–3671, https://doi.org/10.1002/2016JD025617, 2017.

Gerbig, C. and Koch, F.-T.: Biosphere-atmosphere exchange fluxes for CO2 from the Vegetation Photosynthesis and Respiration Model VPRM for 2006-2022, https://doi.org/10.18160/VX78-HVA1, 2021.

Gómez-Ortiz, C., Monteil, G., Basu, S., and Scholze, M.: Can 14CO2 observations help atmospheric inversions constrain the fossil CO2 emission budget of Europe?, EGUsphere, 2023, 1–36, https://doi.org/10.5194/egusphere-2023-2215, 2023.

Gómez-Ortiz, C., Monteil, G., Basu, S., and Scholze, M.: A CO2-Δ14CO2inversion setup for estimating European fossil CO2emissions, Atmospheric Chemistry and Physics, 25, 397–424, https://doi.org/10.5194/ACP-25-397-2025,, 2025.

Graven, H. D.: Impact of fossil fuel emissions on atmospheric radiocarbon and various applications of radiocarbon over this century, Proceedings of the National Academy of Sciences of the United States of America, 112, 9542–9545, https://doi.org/10.1073/PNAS.1504467112/-/DCSUPPLEMENTAL, 2015.

Graven, H. D. and Gruber, N.: Continental-scale enrichment of atmospheric ¹⁴CO₂ from the nuclear power industry: potential impact on the estimation of fossil fuel-derived CO₂, Atmos. Chem. Phys., 11, 12 339–12 349, https://doi.org/10.5194/acp-11-12339-2011, 2011.

Graven, H. D., Guilderson, T. P., and Keeling, R. F.: Observations of radiocarbon in CO2 at seven global sampling sites in the Scripps flask network: Analysis of spatial gradients and seasonal cycles, Journal of Geophysical Research Atmospheres, 117, https://doi.org/10.1029/2011JD016535;REQUESTEDJOURNAL:JOURNAL:21562202D;PAGE:STRING:ARTICLE/CHAPTER, 2012.

Hersbach, H., Bell, B., Berrisford, P., Hirahara, S., Horányi, A., Muñoz-Sabater, J., Nicolas, J., Peubey, C., Radu, R., Schepers, D., Simmons, A., Soci, C., Abdalla, S., Abellan, X., Balsamo, G., Bechtold, P., Biavati, G., Bidlot, J., Bonavita, M., De Chiara, G., Dahlgren, P., Dee, D., Diamantakis, M., Dragani, R., Flemming, J., Forbes, R., Fuentes, M., Geer, A., Haimberger, L., Healy, S., Hogan, R. J., Hólm, E., Janisková, M., Keeley, S., Laloyaux, P., Lopez, P., Lupu, C., Radnoti, G., de Rosnay, P., Rozum, I., Vamborg, F., Villaume, S., and Thépaut, J. N.: The ERA5 global reanalysis, Quarterly Journal of the Royal Meteorological Society, 146, 1999–2049, https://doi.org/10.1002/QJ.3803, 2020.

Huijnen, V., Williams, J., Van Weele, M., Van Noije, T., Krol, M., Dentener, F., Segers, A., Houweling, S., Peters, W., De Laat, J., Boersma, F., Bergamaschi, P., Van Velthoven, P., Le Sager, P., Eskes, H., Alkemade, F., Scheele, R., Nédélec, P., and Pätz, H. W.: The global chemistry transport model TM5: Description and evaluation of the tropospheric chemistry version 3.0, Geoscientific Model Development, 3, 445–473, https://doi.org/10.5194/GMD-3-445-2010, 2010.

ICOS RI, Apadula, F., Arnold, S., Bergamaschi, P., Biermann, T., Chen, H., Colomb, A., Conil, S., Couret, C., Cristofanelli, P., De Mazière, M., Delmotte, M., Di Iorio enea, T., Emmenegger, L., Forster, G., Frumau, A., Haszpra, L., Hatakka, J., Heliasz, M., Heltai, D., Hensen, A., Hermansen, O., Hoheisel, A., Kneuer, T., Komínková, K., Kubistin, D., Larmanou, E., Laurent, O., Laurila, T., Lehner, I., Lehtinen, K., Leskinen, A., Leuenberger, M., Levula, J., Lindauer, M., Lopez, M., Lund Myhre, C., Lunder, C., Mammarella, I., Manca, G., Manning, A., Marek, M. V., Marklund, P., Meinhardt, F., Molnár, M., Mölder, M., Müller-Williams, J., O'Doherty, S., Ottosson-Löfvenius, M., Piacentino, S., Pichon, J.-M., Pitt, J., Platt, S. M., Plaß-Dülmer, C., Ramonet, M., Rivas-Soriano, P., Roulet, Y.-A., Scheeren, B., Schmidt, M., Schumacher, M., Sferlazzo, D., Sha, M. K., Smith, P., Stanley, K., Steinbacher, M., Sørensen, L. L., Trisolino, P., Vítková, G., Yver-Kwok, C., Zazzeri, G., di Sarra, A., ICOS ATC-Laboratoires des Sciences du Climat et de L'Environnement (LSCE) France, ICOS Central Radiocarbon Laboratory (CRL) Germany, and ICOS Flask And Calibration Laboratory (FCL) Germany: ICOS Atmosphere Release 2024-1 of Level 2 Greenhouse Gas Mole Fractions of CO2, CH4, N2O, CO, meteorology and 14CO2, and flask samples analysed for CO2, CH4, N2O, CO, H2, SF6 and 14C, https://doi.org/10.18160/0F1E-DKXT, 2024.

Janssens-Maenhout, G., Crippa, M., Guizzardi, D., Muntean, M., Schaaf, E., Dentener, F., Bergamaschi, P., Pagliari, V., Olivier, J. G. J., Peters, J. A. H. W., van Aardenne, J. A., Monni, S., Doering, U., Petrescu, A. M. R., Solazzo, E., and Oreggioni, G. D.: EDGAR v4.3.2 Global Atlas of the three major greenhouse gas emissions for the period 1970–2012, Earth Syst. Sci. Data, 11, 959–1002, https://doi.org/10.5194/essd-11-959-2019, 2019.

Koch, F.-T. and Gerbig, C.: European anthropogenic CO2 emissions based on EDGARv4.3 and BP statistics 2023 for 2005-2022, https://doi.org/10.18160/RFJD-QV8J, 2023.

Kuderer, M., Hammer, S., and Levin, I.: The influence of 14CO2 releases from regional nuclear facilities at the Heidelberg 14CO2 sampling site (1986-2014), Atmospheric Chemistry and Physics, 18, 7951–7959, https://doi.org/10.5194/ACP-18-7951-2018, 2018.

Kutschera, W.: THE VERSATILE USES OF THE 14C BOMB PEAK, Radiocarbon, 64, 1295–1308, https://doi.org/10.1017/RDC.2022.13, 2022.

Lehmuskoski, J., Vasama, H., Hämäläinen, J., Hokkinen, J., Kärkelä, T., Heiskanen, K., Reinikainen, M., Rautio, S., Hirvelä, M., and Genoud, G.: On-Line Monitoring of Radiocarbon Emissions in a Nuclear Facility with Cavity Ring-Down Spectroscopy, Analytical Chemistry, 93, 16 096–16 104, https://doi.org/10.1021/acs.analchem.1c03814, 2021.

Levin, I. and Kromer, B.: The Tropospheric 14CO2 Level in Mid-Latitudes of the Northern Hemisphere (1959–2003), Radiocarbon, 46, 1261–1272, https://doi.org/10.1017/S0033822200033130, 2004.

Levin, I., Kromer, B., Schmidt, M., and Sartorius, H.: A novel approach for independent budgeting of fossil fuel CO2 over Europe by 14CO2 observations, Geophysical Research Letters, 30, 2194, https://doi.org/10.1029/2003GL018477, 2003.

Levin, I., Karstens, U., Eritt, M., Maier, F., Arnold, S., Rzesanke, D., Hammer, S., Ramonet, M., Vítková, G., Conil, S., Heliasz, M., Kubistin, D., and Lindauer, M.: A dedicated flask sampling strategy developed for Integrated Carbon Observation System (ICOS) stations based on CO2 and CO measurements and Stochastic Time-Inverted Lagrangian Transport (STILT) footprint modelling, Atmos. Chem. Phys., 20, 11 161–11 180, https://doi.org/10.5194/acp-20-11161-2020, 2020.

Lingenfelter, R. E.: Production of carbon 14 by cosmic-ray neutrons, Reviews of Geophysics, 1, 35–55, https://doi.org/10.1029/RG001I001P00035, 1963.

Mahadevan, P., Wofsy, S. C., Matross, D. M., Xiao, X., Dunn, A. L., Lin, J. C., Gerbig, C., Munger, J. W., Chow, V. Y., and Gottlieb, E. W.: A satellite-based biosphere parameterization for net ecosystem CO2 exchange: Vegetation Photosynthesis and Respiration Model (VPRM), Global Biogeochemical Cycles, 22, https://doi.org/https://doi.org/10.1029/2006GB002735, 2008.

Maier, F., Gerbig, C., Levin, I., Super, I., Marshall, J., and Hammer, S.: Effects of point source emission heights in WRF-STILT: a step towards exploiting nocturnal observations in models, Geoscientific Model Development, 15, 5391–5406, https://doi.org/10.5194/GMD-15-5391-2022, 2022.

Maier, F., Levin, I., Gachkivskyi, M., Rödenbeck, C., and Hammer, S.: Estimating regional fossil fuel CO2 concentrations from 14CO2 observations: challenges and uncertainties, Philosophical Transactions of the Royal Society A, 381, https://doi.org/10.1098/RSTA.2022.0203, 2023.

Monteil, G. and Scholze, M.: Regional CO2 inversions with LUMIA, the Lund University Modular Inversion Algorithm, v1.0, Geosci. Model Dev., 14, 3383–3406, https://doi.org/10.5194/gmd-14-3383-2021, 2021.

Monteil, G., Broquet, G., Scholze, M., Lang, M., Karstens, U., Gerbig, C., Koch, F.-T., Smith, N. E., Thompson, R. L., Luijkx, I. T., White, E., Meesters, A., Ciais, P., Ganesan, A. L., Manning, A., Mischurow, M., Peters, W., Peylin, P., Tarniewicz, J., Rigby, M., Rödenbeck, C., Vermeulen, A., and Walton, E. M.: The regional European atmospheric transport inversion comparison, EUROCOM: first results on European-wide terrestrial carbon fluxes for the period 2006–2015, Atmos. Chem. Phys., 20, 12 063–12 091, https://doi.org/10.5194/acp-20-12063-2020, 2020.

Munassar, S., Monteil, G., Scholze, M., Karstens, U., Rödenbeck, C., Koch, F.-T., Totsche, K. U., and Gerbig, C.: Why do inverse models disagree? A case study with two European CO ₂ inversions, Atmospheric Chemistry and Physics, 23, 2813–2828, https://doi.org/10.5194/acp-23-2813-2023, 2023.

Oda, T. and Maksyutov, S.: ODIAC Fossil Fuel CO2 Emissions Dataset (Version name: ODIAC2020b), https://doi.org/10.17595/20170411.001, 2020.

Oda, T., Maksyutov, S., and Andres, R. J.: The Open-source Data Inventory for Anthropogenic CO2, version 2016 (ODIAC2016): a global monthly fossil fuel CO2 gridded emissions data product for tracer transport simulations and surface flux inversions, Earth Syst. Sci. Data, 10, 87–107, https://doi.org/10.5194/essd-10-87-2018, 2018.

Pisso, I., Sollum, E., Grythe, H., Kristiansen, N. I., Cassiani, M., Eckhardt, S., Arnold, D., Morton, D., Thompson, R. L., Groot Zwaaftink, C. D., Evangeliou, N., Sodemann, H., Haimberger, L., Henne, S., Brunner, D., Burkhart, J. F., Fouilloux, A., Brioude, J., Philipp, A., Seibert, P., and Stohl, A.: The Lagrangian particle dispersion model FLEXPART version 10.4, Geosci. Model Dev., 12, 4955–4997, https://doi.org/10.5194/gmd-12-4955-2019, 2019.

Rayner, P. J., Michalak, A. M., and Chevallier, F.: Fundamentals of data assimilation applied to biogeochemistry, Atmospheric Chemistry and Physics, 19, 13 911–13 932, https://doi.org/10.5194/ACP-19-13911-2019,, 2019.

Rödenbeck, C., Gerbig, C., Trusilova, K., and Heimann, M.: A two-step scheme for high-resolution regional atmospheric trace gas inversions based on independent models, Atmospheric Chemistry and Physics, 9, 5331–5342, https://doi.org/10.5194/ACP-9-5331-2009, 2009.

Rödenbeck, C., Keeling, R. F., Bakker, D. C. E., Metzl, N., Olsen, A., Sabine, C., and Heimann, M.: Global surface-ocean p^{CO₂} and sea–air CO₂ flux variability from an observation-driven ocean mixed-layer scheme, Ocean Sci., 9, 193–216, https://doi.org/10.5194/os-9-193-2013, 2013.

Rödenbeck, C., Devries, T., Hauck, J., Le Quéré, C., and Keeling, R. F.: Data-based estimates of interannual sea-Air CO2 flux variations 1957-2020 and their relation to environmental drivers, Biogeosciences, 19, 2627–2652, https://doi.org/10.5194/BG-19-2627-2022, 2022.

Smith, B., Wårlind, D., Arneth, A., Hickler, T., Leadley, P., Siltberg, J., and Zaehle, S.: Implications of incorporating N cycling and N limitations on primary production in an individual-based dynamic vegetation model, Biogeosciences, 11, 2027–2054, https://doi.org/10.5194/bg-11-2027-2014, 2014.

Steinbach, J., Gerbig, C., Rödenbeck, C., Karstens, U., Minejima, C., and Mukai, H.: The CO₂ release and Oxygen uptake from Fossil Fuel Emission Estimate (COFFEE) dataset: effects from varying oxidative ratios, Atmos. Chem. Phys., 11, 6855–6870, https://doi.org/10.5194/acp-11-6855-2011, 2011.

Storm, I., Maier, F., Levin, I., Preunkert, S., and Karstens, U.: Annual emission totals of 14CO2 from nuclear facilities, https://hdl.handle.net/11676/Qa5PvLgEeiXW3IRAfTU5d_Oo, 2024.

Sweeney, C., Gloor, E., Jacobson, A. R., Key, R. M., McKinley, G., Sarmiento, J. L., and Wanninkhof, R.: Constraining global air-sea gas exchange for CO2 with recent bomb 14C measurements, Global Biogeochemical Cycles, 21, https://doi.org/10.1029/2006GB002784, 2007.

Thompson, R. L., Broquet, G., Gerbig, C., Koch, T., Lang, M., Monteil, G., Munassar, S., Nickless, A., Scholze, M., Ramonet, M., Karstens, U., van Schaik, E., Wu, Z., and Rödenbeck, C.: Changes in net ecosystem exchange over Europe during the 2018 drought based on atmospheric observations, Philosophical Transactions of the Royal Society B: Biological Sciences, 375, 20190 512, https://doi.org/10.1098/rstb.2019.0512, 2020.

Turnbull, J., Rayner, P., Miller, J., Naegler, T., Ciais, P., and Cozic, A.: On the use of 14CO2 as a tracer for fossil fuel CO2: Quantifying uncertainties using an atmospheric transport model, Journal of Geophysical Research: Atmospheres, 114, https://doi.org/10.1029/2009JD012308, 2009.

Turnbull, J. C., Karion, A., Fischer, M. L., Faloona, I., Guilderson, T., Lehman, S. J., Miller, B. R., Miller, J. B., Montzka, S., Sherwood, T., Saripalli, S., Sweeney, C., and Tans, P. P.: Assessment of fossil fuel carbon dioxide and other anthropogenic trace gas emissions from airborne measurements over Sacramento, California in spring 2009, Atmos. Chem. Phys., 11, 705–721, https://doi.org/10.5194/acp-11-705-2011, 2011.

van der Woude, A., de Kok, R., Luijkx, I., Peters, W., and Smith, N.: High-resolution, near-real-time fluxes over Europe from CTE-HR: ocean fluxes 2020-04, https://hdl.handle.net/11676/VcS2nlfN06qH22RgmCWbPMUA, 2022.

Varga, T., Orsovszki, G., Major, I., Veres, M., Bujtás, T., Végh, G., Manga, L., Jull, A. J. T., Palcsu, L., and Molnár, M.: Advanced atmospheric 14C monitoring around the Paks Nuclear Power Plant, Hungary, Journal of Environmental Radioactivity, 213, 106 138, https://doi.org/https://doi.org/10.1016/j.jenvrad.2019.106138, 2020.

Vogel, F. R., Levin, I., and Worthy, D. E. J.: Implications for Deriving Regional Fossil Fuel CO2 Estimates from Atmospheric Observations in a Hot Spot of Nuclear Power Plant 14CO2 Emissions, Radiocarbon, 55, 1556–1572, https://doi.org/DOI: 10.1017/S0033822200048487, 2013.

Wang, J. S., Oda, T., Kawa, S. R., Strode, S. A., Baker, D. F., Ott, L. E., and Pawson, S.: The impacts of fossil fuel emission uncertainties and accounting for 3-D chemical CO2 production on inverse natural carbon flux estimates from satellite and in situ data, Environmental Research Letters, 15, 085 002, https://doi.org/10.1088/1748-9326/AB9795, 2020.

Wang, Y., Broquet, G., Ciais, P., Chevallier, F., Vogel, F., Wu, L., Yin, Y., Wang, R., and Tao, S.: Potential of European 14CO2 observation network to estimate the fossil fuel CO2 emissions via atmospheric inversions, Atmos. Chem. Phys., 18, 4229–4250, https://doi.org/10.5194/acp-18-4229-2018, 2018.

Wu, Z.: European hourly NEE, GPP and total respiration for 2010-2022 based on LPJ-GUESS (generated in 2023), https://doi.org/10.18160/p52c-1qjm, 2023.

Zazzeri, G., Acuña Yeomans, E., and Graven, H. D.: Global and Regional Emissions of Radiocarbon from Nuclear Power Plants from 1972 to 2016, Radiocarbon, 60, 1067–1081, https://doi.org/DOI: 10.1017/RDC.2018.42, 2018.